

# Robust Imaging of Fault Slip Rates in the Walker Lane and Western Great Basin from GPS Data Using a Multi-Block Model Approach

William Charles Hammond<sup>1</sup>, Corné Kreemer<sup>2,3</sup>, and Geoffrey Blewitt<sup>2</sup>

<sup>1</sup>Affiliation not available

<sup>2</sup>Nevada Geodetic Laboratory Nevada Bureau of Mines and Geology

<sup>3</sup>Nevada Seismological Laboratory University of Nevada

February 28, 2024

1                   **Robust Imaging of Fault Slip Rates in the Walker Lane and Western Great Basin**  
2                   **from GPS Data Using a Multi-Block Model Approach**

3  
4  
5  
6  
7                   William C. Hammond<sup>1</sup>, Corné Kreemer<sup>1,2</sup>, Geoffrey Blewitt<sup>1</sup>  
8  
9

10  
11  
12                   1) Nevada Geodetic Laboratory  
13                   Nevada Bureau of Mines and Geology  
14

15                   2) Nevada Seismological Laboratory  
16                   University of Nevada, Reno  
17                   Reno NV 89557  
18

19                   *whammond@unr.edu*  
20

21  
22  
23                   Revised Draft February, 2024  
24

25  
26  
27                   Key Points:

28                   1. We estimate Walker Lane fault slip rates using a dense filtered and gridded geodetic velocity  
29                   field and a robust multi-block model approach

30                   2. The geodetic slip rates are independent of geologic slip rates, but 80% agree with them to  
31                   within uncertainties

32                   3. The method images off-fault deformation and vertical axis rotations providing more insight  
33                   into how crustal motion drives earthquakes  
34

## 35 **Abstract**

36  
37 The Walker Lane (WL) in the western Great Basin (GB) is an active plate boundary system  
38 accommodating 10-20% of the relative tectonic motion between the Pacific and North American  
39 plates. Its neotectonic framework is structurally complex, having hundreds of faults with various  
40 strikes, rakes, and crustal blocks with vertical axis rotation. Faults slip rates are key parameters  
41 needed to quantify seismic hazard in such tectonically active plate boundaries but modeling them  
42 in complex areas like the WL and GB is challenging. We present a new modeling strategy for  
43 estimating fault slip rates in complex zones of active crustal deformation using data from GPS  
44 networks. The technique does not rely on prior estimates of slip rates from geologic studies, and  
45 only uses data on the surface trace location, dip, and rake. The iterative framework generates  
46 large numbers of block models algorithmically from the fault database to obtain many estimates  
47 of slip rates for each fault. This reduces bias from subjective choices about how discontinuous  
48 faults connect and interact to accommodate strain. Each model iteration differs slightly in block  
49 boundary configuration, but all models honor geodetic and fault data, regularization, and are  
50 kinematically self-consistent. The approach provides several advantages over bespoke models,  
51 including insensitivity to outlier data, realistic uncertainties, explicit mapping of off-fault  
52 deformation, and slip rates that are more objective and independent of geologic slip rates.  
53 Comparisons to the U.S. National Seismic Hazard Model indicate that ~80% of our geodetic slip  
54 rates agree with their geologic slip rates to within uncertainties.

55

## 56 **Plain Language Summary**

57 The Walker Lane is a complex zone of faults in the western Great Basin of the western United  
58 States that experiences frequent earthquakes driven by active plate tectonics. Ground networks

59 of very sensitive GPS stations deployed over the last few decades have collected data showing  
60 where the ground deforms most quickly, and hence where earthquakes are more likely to occur.  
61 Data on how fast faults slip over time is used to inform the public about the distribution and  
62 intensity of the seismic hazard. In this study we present improved data and modeling that  
63 resolve with unprecedented detail the rates, patterns, and styles of active crustal motion, resulting  
64 in better estimates of fault slip rates in the Walker Lane. This work brings the picture of  
65 earthquake potential derived from GPS networks into sharper focus, provides new information  
66 about how plate tectonics works, and will lead to more accurate estimates of seismic hazard that  
67 can help reduce the loss of life and property from earthquakes.

68

## 69 **1. Introduction**

70 In the Walker Lane and western Great Basin east of the Sierra Nevada Mountains active faults  
71 accommodate ~20% of the Pacific/North America plate boundary relative motion (Dokka and  
72 Travis, 1990; Thatcher et al., 1999; Bennett et al., 2003; Oldow, 2003). The fault system is  
73 composed of a complex set of active dextral, sinistral, and normal faults (Stewart, 1988;  
74 Wesnousky, 2005; Faulds and Henry, 2008) that together work to release the accumulating  
75 crustal strain (Figure 1). The faults are numerous, in places closely spaced and discontinuous,  
76 and are linked to regional seismicity (dePolo, 2008; dePolo and dePolo, 2012). The system's  
77 complexity creates a challenge for using measurements of active deformation from GPS geodesy  
78 to estimate the slip rates on the faults.

79

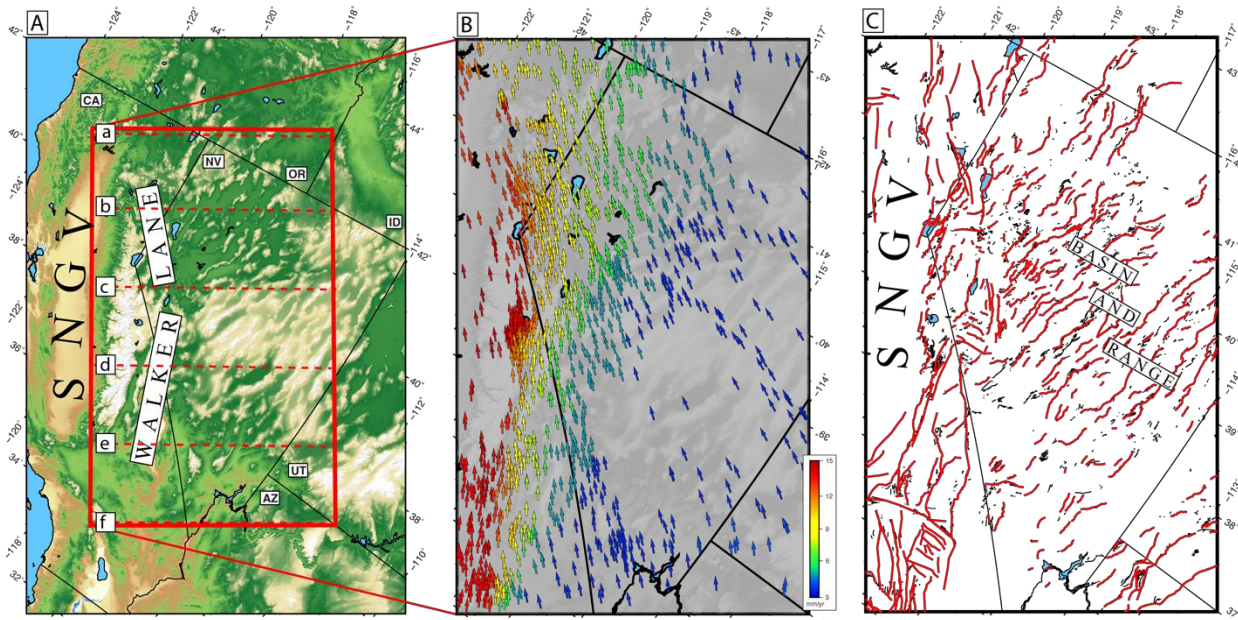
80 Fault slip rates are important for several reasons. For example, rates and azimuths of fault slip  
81 are used to understand the kinematics of tectonics that drive processes within the plate boundary

82 zones (e.g., Weldon and Humphreys, 1986), and are used to compare to results of global plate  
83 tectonic circuits (e.g., deMets and Merkouriev, 2016). Another reason that is of high societal  
84 relevance is that slip rates are used in seismic hazard analysis, such as the US National Seismic  
85 Hazard Maps (NSHM) project. In these hazard models the faults represent sources of elastic  
86 moment that will be released in potentially damaging future ground shaking from earthquakes  
87 (Frankel et al., 2002; Peterson et al., 2014; Field et al., 2023). For all these applications the  
88 accuracy of the faults slip rates is essential.

89

90 However, the problem is challenging owing to gaps in the fundamental datasets, and aleatory and  
91 epistemic uncertainties in those data. Geodetic data can constrain the rate of interseismic strain  
92 accumulation expected to be released in earthquakes but is limited by the short time of  
93 observation (usually one to three decades). Nonetheless, they are a vital complement to other  
94 data such as seismicity and earthquake geology which also constrain hazard (Shen et al., 2007;  
95 Bird, 2009; Kreemer and Young, 2022). These data types each have their own strengths, sources  
96 of uncertainty, community of practice, and offer complementary means for measuring active  
97 crustal deformation. Comparisons between geologic, geodetic, and seismic moment rates reveal  
98 both similarities between, and gaps among, the datasets (Ward, 1998; Pancha et al., 2006),  
99 suggesting that approaches that take advantage of their individual strengths are needed.

100



101 **Figure 1.** A) Walker Lane and western Great Basin Region of the western United States, red box  
 102 indicates area covered in B) and C), red horizontal dashed lines a-f indicate location of profiles shown in  
 103 Figure 2. B) Median spatial filtered velocity field. Vectors are of constant length with color indicating  
 104 magnitude of velocity in a North America reference frame. C) Fault networks representing sources in the  
 105 USGS NSHM (Hatem et al., 2022a) (red) and other Quaternary faults (black). Supplemental Figure S1 is  
 106 a version of C annotated with fault names referred to in the text. SNGV indicates the Sierra  
 107 Nevada/Great Valley microplate.  
 108

109

110 Integrated approaches have been attempted in a recent modeling exercise to support the latest  
 111 version of the US NSHM. A group of expert modelers developed solutions from the same input  
 112 database of western US fault geometries and GPS velocity field. They estimated slip rates for  
 113 faults in the database using their own various methodologies incorporating combinations of  
 114 geologic and geodetic data (Evans, 2022; Pollitz, 2022a; Shen and Bird, 2022; Zeng, 2022a).  
 115 Introduction and review of these models have been provided by Pollitz (2022b) and Johnson et  
 116 al., (2024). They point out that while the slip rate estimates exhibit broad similarity, they differ  
 117 in some important measures owing to multiple factors that sometimes result in high variability.  
 118 In those models the coefficient of variation for slip rates below 5 mm/yr (a category inside which  
 119 all WL faults lie) is above 2.0, indicating lack of agreement among the modelers at the level of

120 the uncertainties. Moreover, all the models incorporate geologic slip rates (Hatem et al., 2022b)  
121 as additional constraints to regularize their inversions and so the resulting estimates are not  
122 independent of geologic rates.

123

124 Here we address the slip rate problem by introducing a new block modeling method where block  
125 geometries are repeatedly generated through a well-defined computational procedure from a  
126 given input fault data base. In each iteration the model starts with many blocks whose number  
127 are iteratively reduced to limit the number of free parameters. These models are generated  
128 automatically in subdomains of the region of interest, iterating with slightly different starting  
129 conditions so that large numbers of slip rate estimates are made for each fault. While each  
130 individual model contains some of the usual errors associated with model construction, the errors  
131 are different for each iteration and so are a noise that is reduced by averaging over many models.  
132 However, the signals of fault slip rates are similar in every model because they are present and  
133 have the same geometry in each iteration. In this way the power of large numbers increases the  
134 robustness of the slip rate estimate to find the set of kinematically consistent slip rate estimates  
135 that fit the data. The technique is like other robust approaches that involve repeated sampling of  
136 the data to achieve estimates of velocity or strain rates (e.g., Blewitt et al., 2016; Kreemer et al.,  
137 2018; Husson et al., 2018).

138

139 The degree of independence that the estimated geodetic rates have from geologic rates is an issue  
140 with the NSHM deformation models identified in recommendations for future efforts (Johnson et  
141 al., 2024). In our method described here geologic data from the NSHM (Hatem et al., 2022a) are  
142 used to define the location, geometry, and style of fault segments, but not their slip rates. Thus,

143 agreements between our geodetic and geologic rates are corroborative, rather than the result of  
144 an analytical constraint that they must be similar.

145

## 146 **2. Velocity Data**

147 We use horizontal position time series from the GPS holdings of the Nevada Geodetic  
148 Laboratory (NGL, Blewitt et al., 2018) which are processed uniformly using the GipsyX  
149 software (Bertiger et al., 2020). RINEX data are from networks listed in the Data Availability  
150 Statement and include stations whose time series have duration longer than 2.5 years. We used  
151 data products including daily reference frame alignment, orbit and clock files that were provided  
152 by the Jet Propulsion Laboratory. More properties of the GPS data processing may be found in  
153 Kreemer et al., (2020) and in the NGL GPS data analysis strategy and products summary  
154 (<http://geodesy.unr.edu/gps/ngl.acn.txt>). We correct the time series for the effects of non-tidal  
155 atmospheric, non-tidal ocean, and hydrological surface mass loading. These corrections have  
156 been shown to reduce noise in GPS time series, especially in the vertical component, but also in  
157 the horizontal component (Chanard et al., 2018; Martens et al., 2020). The corrections are based  
158 on the predictions from the Earth System Modelling Group of GFZ Potsdam (Dill and Dobslaw,  
159 2013), which are provided on a  $0.5^\circ \times 0.5^\circ$  grid and interpolated onto the GPS station locations  
160 and provided on the NGL GPS station pages. The trends of the time series represent motion with  
161 respect to a fixed North American (NA) plate that has an Euler pole of rotation in the  
162 International Terrestrial Reference Frame (Altamimi et al., 2016) defined by Kreemer et al.,  
163 (2014). We obtain trends in station positions from the corrected time series with the MIDAS  
164 robust non-parametric estimator, which is insensitive to steps, seasonality, outliers and  
165 heteroskedasticity in the time series (Blewitt et al., 2016).

166  
167 Additional campaign GPS data are taken from several sources that are listed in the Data  
168 Acknowledgement section. While campaign GPS velocities tend to be less precise than those  
169 from continuous stations, they have been shown in many studies to be precise enough to  
170 constrain crustal movement. They are numerous and dense, enhancing geographic coverage of  
171 the velocity field (e.g., Bennett et al., 1996; Thatcher et al., 1999; Oldow et al., 2003; Hammond  
172 and Thatcher, 2005; McCaffrey et al., 2007; Spinler et al., 2010; Lifton et al., 2013; Murray and  
173 Svarc, 2017, to name a few). We align these velocity solutions into the same North America  
174 reference frame as the NGL MIDAS NA velocity field. Stations in clusters within  $.001^\circ$  of one  
175 another were combined into single rates by taking the median rate of the cluster. We include all  
176 stations within  $1^\circ$  outside the model domain (Figure 1) to help constrain the reference frame  
177 alignments between velocity fields and to reduce edge effects in the analysis that follows.  
178 Together these networks provide 1311 stations inside the domain (421 continuous, 343  
179 MAGNET semi-continuous, 547 campaign) (Figure 1). Like other recent analyses we impose a  
180 velocity uncertainty floor of 0.1 mm/yr for both horizontal components to prevent very low  
181 uncertainty velocities from having a disproportionately large influence on the inversions for slip  
182 rates. Histograms of the east and north component velocities and their uncertainties are provided  
183 in Figures S2 and in map view in Figure 1B and S3. A table of velocities and uncertainties is  
184 provided in the Supplement (Table S1).

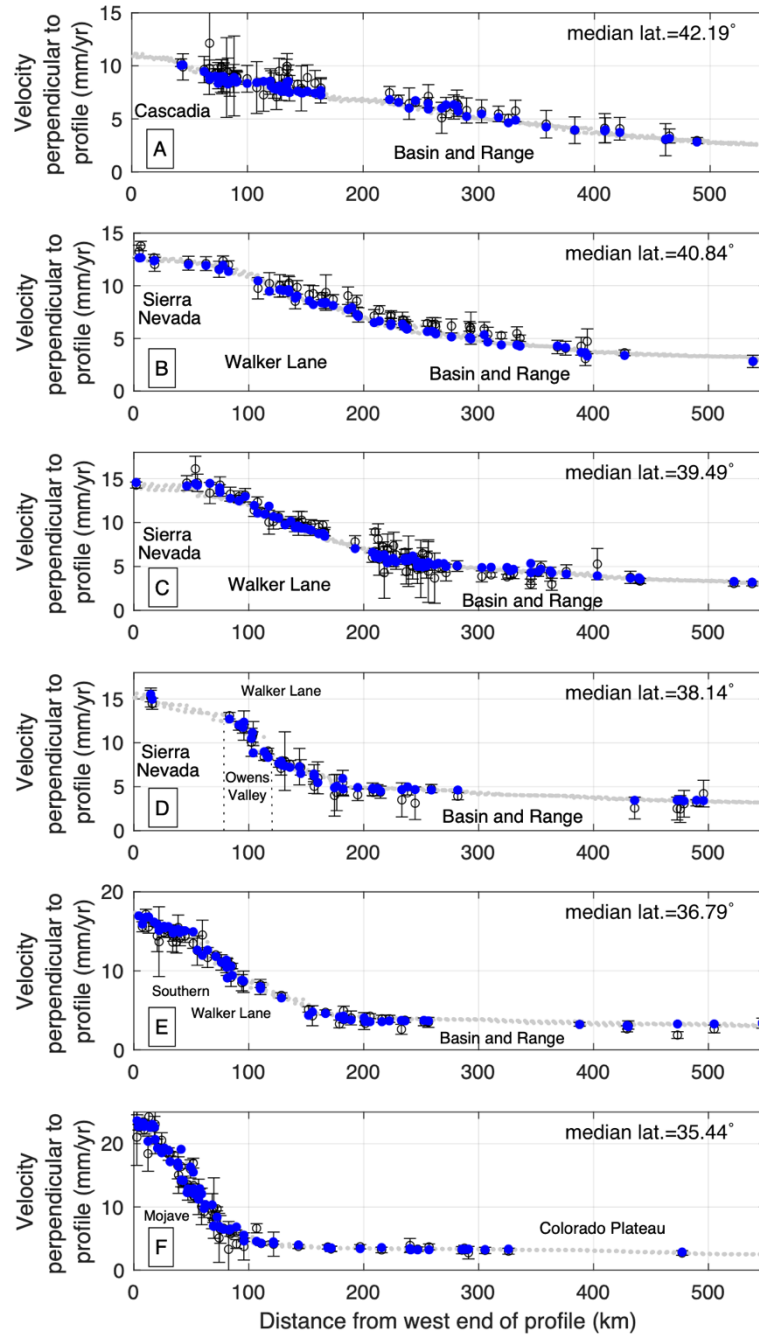
185  
186 To omit outliers and noise from the velocity field we apply median spatial filtering to each  
187 horizontal component. This process replaces each velocity with a weighted median of itself and  
188 its neighbors, where the weight is a function of distance, data uncertainties, and a spatial

189 structure function (Hammond et al., 2016). The same process is used to image the velocities by  
190 estimating at every point on a regular grid (spacing of  $0.045^\circ \times 0.045^\circ$  or  $\sim 5 \times 5$  km) the weighted  
191 median of velocities from the nearest stations. The gridded field is used for the block modeling  
192 because it is representative of the smoothly varying WL velocities and ensures that multiple  
193 velocity estimates are present for even small blocks. The gridded field is shown in Figure S3.

194

195 Six profiles of velocity across the WL normal to the direction of Pacific and North America  
196 relative plate motion show the patterns of the velocities and the magnitude of the signals with  
197 respect to their uncertainties (Figure 2). The location of the 50 km wide profiles is shown in  
198 Figure 1A. The gridded velocity is always within the uncertainty bounds of the station  
199 observations, except in cases with obvious outliers. The profile-perpendicular velocities increase  
200 to the west monotonically and their spatial gradient increases southward as the zone of  
201 accommodation between the GB and WL narrows, consistent with previous studies (Kreemer et  
202 al., 2012).

203



204

205 **Figure 2.** Velocity components perpendicular to the profile locations shown in Figure 1. Original  
 206 velocities are shown with open circles and error bars with 2 times the uncertainties. Larger blue circles  
 207 are the median spatial filtered velocities, the small gray dots are values from the gridded velocity field.  
 208 Velocities parallel to the profile direction are provided in the Supplementary Figure S4. Some geographic  
 209 features are annotated.  
 210  
 211

212 The component of velocity parallel to the profiles (Figure S4) reveals smaller trends that vary  
213 with latitude, which reflect differences in the azimuth of the Sierra Nevada/Great Valley  
214 microplate (SNGV - Figure 1 and S1) motion from south to north. The change in sign of the  
215 trend is related to the rotation of the SNGV microplate, which results in motion away from the  
216 Pacific plate in the south, and motion towards the Pacific plate in the north, consistent with  
217 SNGV counterclockwise rotation (Figure 1B) (e.g., Argus and Gordon, 1998; Dixon et al., 2000;  
218 Bennet et al., 2003). This rotation sets the western boundary condition and exerts a strong  
219 control on the strike and style of faulting east of the SNGV in the WL, which varies from south  
220 to north (Wesnousky, 2005; Wesnousky et al., 2012).

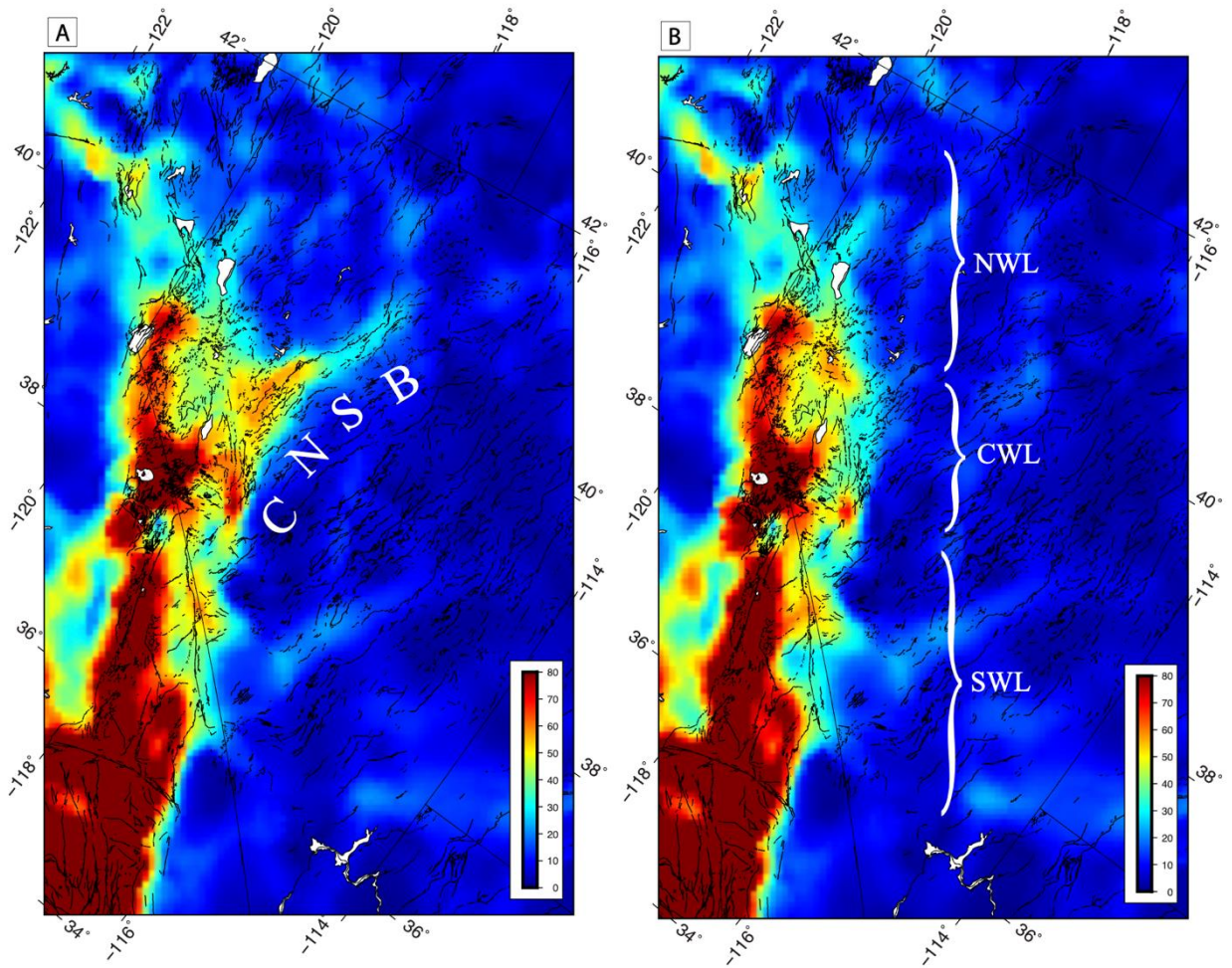
221

## 222 **3. Analysis**

### 223 **3.1 Strain Rates**

224 Maps of the tensor strain rate components of shear and dilatation depict the geographic variation  
225 of strain accumulation which may eventually be released in earthquakes. In the fault slip rate  
226 analysis described below, we use a strain rate map to provide a regularization to the block  
227 modeling. Various kinds of parameterizations and regularizations for building strain rate maps  
228 have been tested and compared (e.g., Beavan and Haines, 2001; Spakman and Nyst, 2002; Tape  
229 et al., 2009; Hearn et al., 2010; Shen et al., 2015; Mauer and Materna, 2023). Our formulation  
230 separates gradients in the GPS velocity field on a sphere into components of tensor deformation  
231 and rotation using the parameterization of Savage et al. (2001). At each grid point we estimate  
232 the local strain rate tensor with a linear inversion from the gridded horizontal velocities as input  
233 data weighted with the velocity uncertainties. The results are insensitive to outlier velocity data  
234 and irregularities in station spacing because the velocities have been spatially filtered and

235 gridded. Based on the result of an analysis of trade-off between high spatial resolution and low  
 236 data misfit (Supplemental text and Figure S5) we adopted a length scale of 8 km for the shear  
 237 and dilatational component strain rate maps (Figure 3). We depict the shear as the difference  
 238 between principal strain rates ( $\dot{\epsilon}_1 - \dot{\epsilon}_2$ ) and dilatation as the sum of principal strain rates ( $\dot{\epsilon}_1 +$   
 239  $\dot{\epsilon}_2$ ) (Figure 3).  
 240



241  
 242 **Figure 3.** A) Shear strain rates ( $\dot{\epsilon}_1 - \dot{\epsilon}_2$ ), color scale is in nanostrains ( $10^{-9}$ ) per year. White "C N S B"  
 243 indicates strain rate anomaly associated with Central Nevada Seismic Belt earthquakes. B) Same map  
 244 except with correction applied for viscoelastic postseismic relaxation from all the CNSB earthquakes  
 245 modeled by Hammond et al., (2009). Black lines are Quaternary faults. Approximate extent of Southern  
 246 (SWL), Central (CWL) and Northern Walker Lane (NWL) according to Faulds and Henry, (2008) are  
 247 indicated with white curly braces. Fault names are given in Supplemental Figure S1.  
 248

249 The contiguous band of high strain rates east of the SNGV is the geodetic signal of the WL, its  
250 intensity decreases from south to the north. Its lower intensity in the Northern Walker Lane  
251 (NWL) is a function of the wider and shallower gradient in GPS velocity compared to the  
252 Southern Walker Lane (SWL) profiles (see B, C, D and E in Figures 1 and 2). The total velocity  
253 difference across the system decreases from  $\sim 10$  mm/yr in the SWL to  $\sim 7$  mm/yr in the NWL.  
254 Hence strain rates increase southward as a larger total velocity budget is accommodated across a  
255 narrower zone.

256

257 We discuss other features of the WL strain rate maps in parts:

258

259 *In the Southern WL (SWL)* there are significantly higher strain rates in the Owens Valley ( $>80 \times$   
260  $10^{-9}$ /yr) adjacent to the eastern SNGV than there are along other fault systems of the eastern WL  
261 such as Death Valley, Furnace Creek, Fish Lake Valley, and Panamint Valley (see Figure S1 for  
262 map with fault names). This is attributable to the higher gradient in GPS velocities adjacent to  
263 the SNGV (see profile D of Figure 2). Strain rates across the Owens Valley are strongly  
264 transtensional, as seen in the relatively high shear strain rate (Figure 3) and positive dilatation  
265 rates (Figure 4). This is consistent with the strike of the Owens Valley ( $\sim N20^\circ W$ ) being in a  
266 releasing geometry with respect to azimuth of SNGV motion ( $\sim N50^\circ W$ ) (as noted by Unruh et  
267 al., 2003). The higher strain rates are more concentrated in the northern sections of the Owens  
268 Valley Fault and widen to the south to distribute deformation more evenly across the southern  
269 Sierra Nevada, Little Lake, Airport Lake, Panamint Valley, and southern section of the Death  
270 Valley Fault. The Death Valley/Fish Lake Valley fault system has lower strain rates ( $30\text{-}60 \times 10^{-9}$   
271 /yr) but are still elevated above the rates in the GB east of the WL.

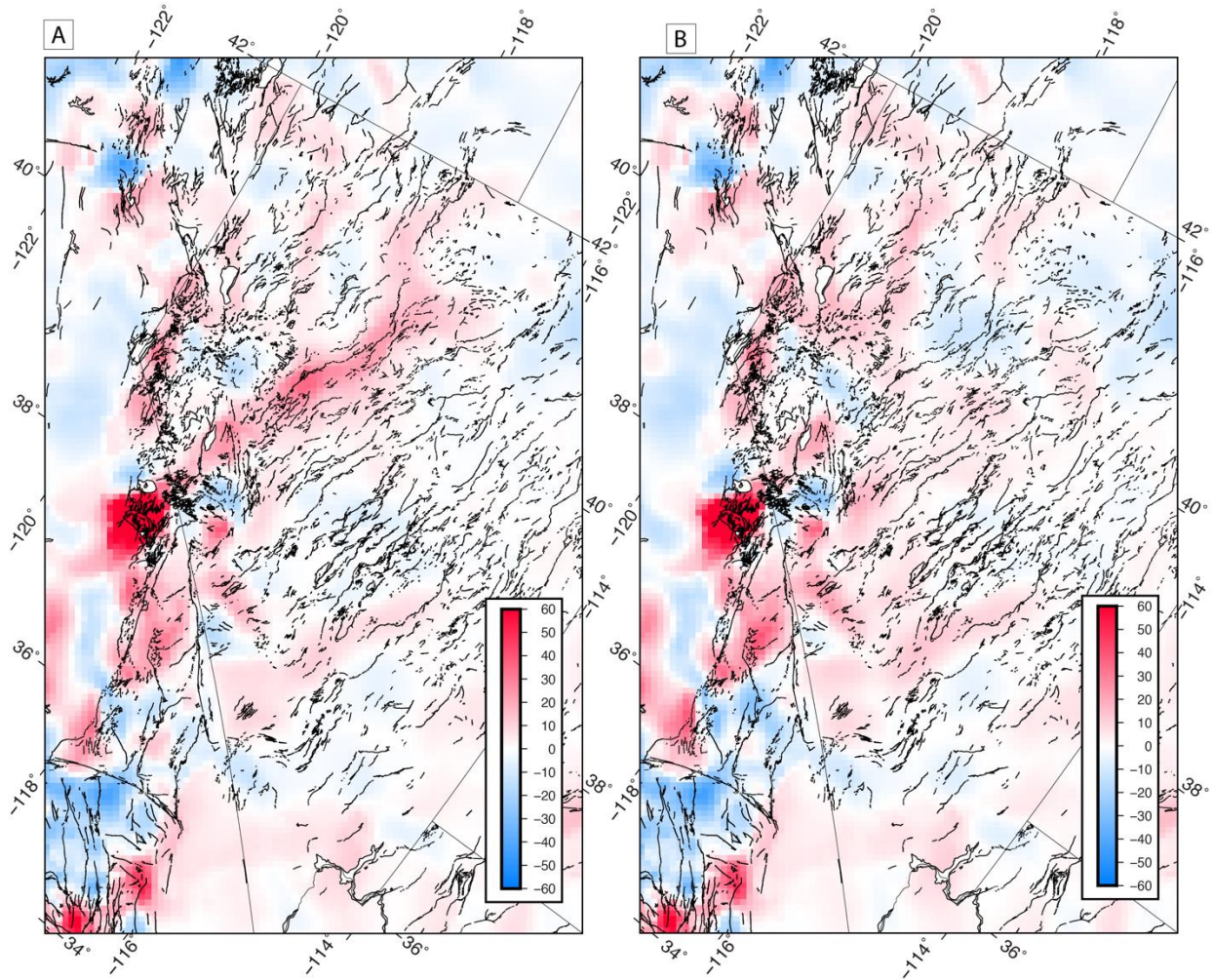
272  
273 *In the Central WL (CWL)* the location and width of the zone of highest strain rates varies with  
274 latitude. Just north of the SWL, the shear steps left and concentrates, passing through the Long  
275 Valley Caldera near the SNGV (shown in detail in Hamond et al., 2019) and then widens again  
276 northward. Here the higher shear strain rates occupy all the area between the SNGV and  
277 northwest striking dextral fault systems east of Walker Lake such as Petrified Spring, Benton  
278 Spring, and Gumdrop Hills faults (Wesnousky, 2005; Angster et al., 2020). However, shear rates  
279 are highest at the east and west margins of the CWL, near the SNGV and east of the Wassuk  
280 Fault. However, dilatation rates (Figure 4A) show faster extension near the western margin  
281 adjacent to the SNGV and the Wassuk Fault. This is consistent with the partitioning between  
282 shear and extensional domains (Surpless, 2008). However, it may be only a matter of degree  
283 because the shear rates are lower west of the Wassuk but not zero, and the analyses of Bormann  
284 et al., (2016) suggests that some strike slip through this part of the CWL is required to explain  
285 the GPS data. At the left lateral faults in the Mina Deflection such as the Rattlesnake, Excelsior,  
286 Candelaria Hills faults the shear strain rates are lower ( $40 - 60 \times 10^{-9}/\text{yr}$ ) than those closer to the  
287 SNGV, but are still higher than those in the GB to the east, where the strain rates drop  
288 precipitously to below  $10 \times 10^{-9}/\text{yr}$ .

289  
290 *In the Northern WL (NWL)* the strain rates separate and focus into two main arms, one in the  
291 westernmost NWL overlapping the Lake Tahoe Basin adjacent to the SNGV, and the other  
292 extending north-northeast to follow the Fairview, Dixie Valley and Pleasant Valley faults. This  
293 zone is the location of a sequence of earthquakes that released most of the seismic moment in the  
294 GB in the 20th century, known as the Central Nevada Seismic Belt (CNSB). In the next section

295 we discuss the transient nature of this active deformation feature. North of Lake Tahoe the NWL  
296 shear strain rates are lower ( $\sim 40 \times 10^{-9}/\text{yr}$ ) than to the south ( $>80 \times 10^{-9}/\text{yr}$ ) and confined to a  
297 narrow zone between the Pyramid Lake and Mohawk Valley Faults, narrowing even further  
298 north to lie between the Eagle Lake and Almanor Faults. Further north still a pocket of medium-  
299 high strain rates ( $\sim 50 \times 10^{-9}/\text{yr}$ ) lies at the Inks Creek, Battle Creek, and Bear Creek faults, a  
300 place that may represent the locus of active convergence between the SNGV and crustal blocks  
301 in the southern Cascadia forearc (Unruh et al. 2017; Angster et al., 2020).

302

303 *Along the east edge of the WL* eastward protrusions of elevated strain rates occur near locations  
304 of east-northeast striking left-lateral faults such as in the Carson Domain near the Olinghouse  
305 Fault, Mina Deflection, Gold Mountain east of the Death Valley Fault, and the Rock Valley Fault  
306 south of Yucca Mountain. The Clayton Valley and Lone Mountain faults also have rates  
307 slightly elevated compared to the rest of the GB east of the Death Valley fault, consistent with  
308 the findings of Lifton et al., (2013) who detected extension normal to strike near the level of the  
309 uncertainties with campaign GPS. The evolution of these faults may be linked to the nearby  
310 strike slip systems of Fish Lake Valley/Death Valley (Oldow et al., 1994), suggesting that  
311 perhaps all these protrusions are similar cases with similar mechanical origin. Significant strain  
312 rates protruding east of the WL, elevated above background GB rates have been seen in other  
313 recent strain rate models as well (e.g., Zeng, 2022b), and are especially apparent in maps made  
314 with combinations of geodetic and geologic data (Kreemer and Young, 2022). These signals  
315 may indicate that complexities exist in the deformation field in the GB east of the WL but are  
316 currently near the resolution of the geodetic data, which may be clarified with better geodetic  
317 coverage east of the WL and/or longer time series.



319

320 **Figure 4.** Same as Figure 3A and 3B except for dilatational strain rate ( $\dot{\epsilon}_1 + \dot{\epsilon}_2$ ), C) without correction  
 321 for postseismic deformation, D) with correction.

322

323

324 *Inside the SNGV* strain rates are very low (mostly  $<10 \times 10^{-9}/\text{yr}$ ), consistent with previous  
 325 geodetic studies (Argus and Gordon, 1998; Dixon et al., 2000; Bennet et al., 2003; Kreemer et  
 326 al., 2012), lower levels of seismicity and sparsity of faults in the compilations (Figure 1C and  
 327 S1). The boundary between the low strain rates in the SNGV and the high strain rates in the WL  
 328 is very near the faults bounding the SNGV east edge. The most significant exception to the

329 SNGV rigidity is in the southernmost part of the microplate west of the SWL and Owens Valley,  
330 where the Kern Canyon, Lake Isabella and western extension of the White Wolf faults extend  
331 north of the Garlock fault into the High Sierra. Seismicity in this area has been used to suggest  
332 that the southernmost Sierra is subject to heterogenous extension and crustal thinning associated  
333 with foundering of lower lithosphere (Unruh et al., 2014).

334

335 The dilatational strain rate field indicates rates of area change that are generally lower than shear  
336 strain rates (Figure 4AB) but are positive on average consistent with the WL and GB being a  
337 transtensional part of the PA/NA plate boundary system. Owing to smaller signal to noise ratio  
338 dilatation rate is harder to resolve than shear rate in the WL, but some clear patterns emerge.

339 Rates are faster in the WL than in the GB, and the stripe of faster extension adjacent to the Sierra  
340 Nevada coincides with a zone of extension-dominated transtension noted by Oldow (2003).

341 Strong positive dilatation is observed near the Long Valley Caldera active magmatic system that  
342 is undergoes episodic inflation (Montgomery-Brown et al., 2015). This inflation affects a  
343 volume of crust with active strain penetrating westward into the SNGV and eastward into the  
344 WL, influencing seismicity which is transient deformation possibly not representative of long-  
345 term deformation (Hammond et al., 2019).

346

### 347 **3.2 Correction for Viscoelastic Postseismic Relaxation**

348 Some signals in the geodetic data are not representative of the long-term rate and pattern of  
349 deformation and must be removed from the velocity field before estimating time-invariant slip  
350 rates. In the WL and western GB signals from post-earthquake relaxation related to the late 19th  
351 and 20th century M 6.9-7.5 earthquakes in the Central Nevada Seismic Belt (CNSB) (Wallace,

352 1984; Bell et al., 2004) are apparent in the geodetic data. It has been shown in several studies  
353 that these earthquakes initiated uplift and dilatation anomalies in central Nevada, which stand out  
354 from the slow background rates in the rest of the Basin and Range (Gourmelen and Amelung,  
355 2005). We use a model of the viscoelastic relaxation process for the CNSB (Hammond et al,  
356 2009) using the theory and software of Pollitz (1997) to subtract the transient anomaly from the  
357 measured velocities. The model accounts for the effects of nine earthquakes that occurred east of  
358 the SNGV and within our area of study including the 1872 Owens Valley M7.4, 1915 Pleasant  
359 Valley M7.3, 1954 Dixie Valley M6.9, 1954 Fairview Peak 7.0. The strain rates predicted from  
360 the relaxation model have concentrations of both shear and dilatation owing to the obliquity of  
361 the ruptures and uniaxial component of extension at the CNSB. The predictions illustrated in  
362 Figure S6 were interpolated to the same GPS stations used in this analysis, subject to the same  
363 GPS Imaging process before tensor strain rates are calculated, and mapped with the same bounds  
364 as Figures 3 and 4. There are uncertainties in the relaxation model associated with limits of our  
365 knowledge of the slip during these past earthquakes as well as in the structure and rheology of  
366 the Walker Lane crust and mantle. However, the model is based on seismic and geologic data  
367 and estimates crust and mantle viscosities similar to those found in other studies in the western  
368 United States. Details of model construction are provided in Hammond et al., (2009) which  
369 includes description of the rheological assumptions that were made, how it is derived from  
370 earthquake parameters. Another indication that this model is reasonable is that the strain rate  
371 field corrected for CNSB postseismic relaxation removes the long finger-shaped anomaly of high  
372 shear and dilatational strain rate that branches north-northeast from the main band of high strain  
373 rates northeast of the CWL (Figure 4A and B). In the corrected strain rate maps the eastern

374 boundary of the higher strain rates in the WL becomes much straighter and more parallel to its  
375 western boundary (Figure 3B).

376

377 While the model removes the single most obvious north-northeast trending anomaly, we notice  
378 the existence of several other lower intensity anomalies that extend in a similar direction to the  
379 CSNB anomaly, but are not corrected by the relaxation model. One is near Pyramid Lake, NV  
380 and the other near Eagle Lake, CA, west of the CNSB. Whether these reveal the unmodeled  
381 effects of earthquakes occurring further in the past is unknown. However, it is likely that not all  
382 events occurring in the last 1000 years on WL faults are documented. Paleoseismic data show,  
383 however, that an event with  $\sim 3.3$  m of slip occurred on the Incline Village Fault in the northern  
384 Lake Tahoe Basin  $\sim 500 \pm 150$  years before present (Seitz et al., 2016). The amount of offset and  
385 length of the fault suggests a magnitude of  $\sim 7.1$ . That would have been enough seismic moment  
386 to generate a postseismic viscoelastic signal that is detectable with GPS, as in the CNSB.  
387 Whether that signal persists to the present day and is related to the observed strain rate anomalies  
388 is speculative. There are other low amplitude strain rate anomalies in both the shear and  
389 dilatation fields that are noticeable east of the WL, where background strain rates are lower.  
390 However, some of these may be related to artifacts in the imaging technique.

391

392 We do not attempt to correct the GPS velocity field for the magmatic inflation at LVC because  
393 volcanic deformation is not a cyclic effect as is the case for faults. Inflation-related deformation  
394 may be cumulative and influence nearby faults so should be modeled as part of the strain  
395 accumulation field, and related slip rates.

396

397

### 398 **3.3 Block Modeling**

#### 399 3.3.1. Justification for the approach

400 Block modeling assumes that the crust is divided into contiguous moving elastic volumes that  
401 drive slip on the faults that bound them. The method accounts for the fact that the data are  
402 collected during the interseismic period when fault systems are locked from the surface to the  
403 bottom of the seismogenic upper crust but slip at the block motion rate at greater depth. The  
404 parameterization enforces kinematic consistency between fault slip rates and crustal block  
405 translation and rotation. Several implementations have been developed, varying in  
406 parameterization, complexity, and use of regularization (e.g., Savage and Burford, 1973;  
407 Matsu'ura et al., 1986; Bennett et al., 1996; McCaffrey, 2002; Meade and Hagar, 2005; Loveless  
408 and Meade, 2010; Evans et al, 2015).

409  
410 In the WL a system-scale block modeling approach is particularly needed because there are  
411 many faults that together form network which creates a complex distribution of seismic hazard.  
412 Block modeling represents the complexity in the network of faults with a framework that allows  
413 integration of several kinds of data to understand the system. Block modeling is, however,  
414 challenging for a couple of reasons. First, vertical-axis rotations of crustal blocks are observed in  
415 the Walker Lane and these rotations are intimately linked to the fault slip. While paleomagnetic  
416 data constrain rotation since 10-13 Ma for some blocks (Cashman and Fontaine, 2000; Petronis  
417 et al., 2009; Carlson et al., 2013), their present-day rates of rotation are not well known, and data  
418 is not available for all WL areas. Given the spacing between faults (5-30 km) and locking depths  
419 (~15 km) the signals of elastic strain accumulation and rotation across the blocks spatially  
420 overlap. This leads to the solution for block rotations and slip rates to be under-determined, with

421 trade-offs between parameters. Regulation of the problem is required, and our approach to this is  
422 explained below. Second, the large number of faults and complexity of the fault system (Figure  
423 1C) make manual building of traditional block models cumbersome. Block models generally  
424 require completely connected boundaries that define independent polygonal domains. However,  
425 it is not always possible to define the boundaries objectively because mapped fault traces are  
426 discontinuous, may be based on incomplete datasets, and must be drawn according to subjective  
427 decisions from the analyst. We address this difficulty in the next section.

428

### 429 3.3.2. Automated and iterative block model generation

430 Here we describe the procedure for generating block models from a database of faults. To begin  
431 we require that each fault in the database be represented by an ordered sequence of coordinates  
432 that define the surface trace and the fault dip. We use the NSHM database of western US faults  
433 (Hatem et al., 2022a) which provides these parameters. There are 373 faults in the database that  
434 touch the study domain for which we estimate a slip rate (Figure 1). While not every known  
435 fault in the GB is represented in this database, it includes the structures that are best studied and  
436 have demonstrated Quaternary activity.

437

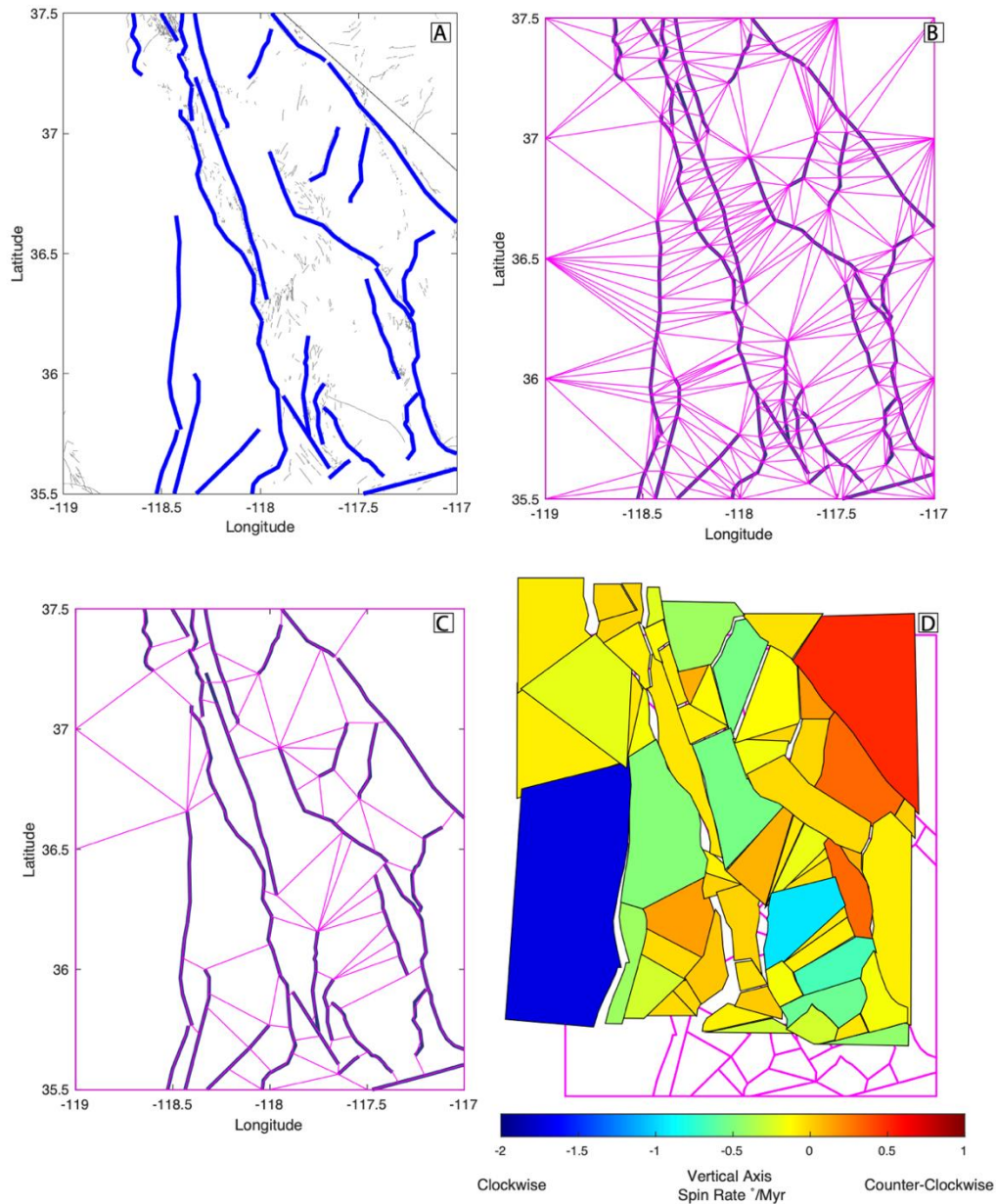
438 Prior to constructing each block model the fault traces are further simplified beyond the already  
439 simplified traces available in the NSHM database (Hatem et al., 2022c). We select a subdomain  
440 consisting of a latitude/longitude box of  $2^\circ \times 2^\circ$  and truncate the fault traces to include only those  
441 segments inside the box (Figure 5). We also down-sample the number of nodes used to define  
442 fault traces so that each segment has length no smaller than  $\sim$ one fortieth of the dimension of the  
443 subdomain ( $0.05^\circ$ ). The spacing of segment nodes is controlled because they define seed

444 locations for the next step which is the generation of an initial set of blocks. Nodes on the  
445 rectangular boundaries of each model are needed so that blocks can extend to the edge of the  
446 domain. We place one at each corner and 3 more along each side so that the initial configuration  
447 has blocks that are small enough to represent fault geometries. The result is a set of nodes on the  
448 faults and boundaries that define a Delaunay triangulation where every fault segment is the side  
449 of one of the triangles. Associating each fault segment with a triangle side makes a valid block  
450 model that honors the fault network (Figure 5B). However, this model is primitive because the  
451 presence of many small and narrow blocks makes it poorly parameterized for deformation  
452 modeling. The model suffers from an excessive number of free parameters (3 Euler rotation  
453 vectors for each block) and the block rotations are difficult to constrain with GPS velocity  
454 gradients because block dimensions may be small in one or more directions.

455  
456 We reduce the number of blocks in the model by joining selected abutting block pairs into single  
457 blocks and repeating the process iteratively. Since each block is represented by an ordered  
458 sequence of node numbers, two blocks are abutting if they share a subset of nodes. Removing  
459 the boundary between two blocks involves deleting them and then adding a new one composed  
460 of the polygonal union of the original two. At each iteration we prioritize which block pairs to  
461 combine by developing a ranking system, where block bounding segments are scored according  
462 to their geometric properties. Segments with low scores are selected for elimination, and the two  
463 adjacent blocks are joined into one. Block boundary segments that align with faults are given  
464 score of infinity so they cannot be lost through joining of blocks. Segments that are aligned with  
465 the domain boundary are also given score of infinity. Segments that otherwise touch faults are  
466 given a score equal to the number of fault segments touched, which preserves some detail in the

467 model near faults, but also allows for simplification so that individual segments along a fault  
468 tend to have similar slip rates. Blocks are also targeted for combination if they have very small  
469 angles at vertices ( $20^\circ$  or less), small area ( $100 \text{ km}^2$  or less), large shape parameter defined as the  
470 perimeter divided by the square root of the area (10 or more, where a circle is  $\sim 3.5$ ), or large  
471 interior angles ( $190^\circ$  or more) which prevents blocks with significant concavity. Also blocks  
472 having more than one contiguous chain of boundary nodes ('doughnut blocks') are forbidden by  
473 not allowing any block merging that results in this condition. An example of a block number  
474 reduction operation sequence is shown in Figure 5. The systematic joining of many small  
475 blocks into fewer larger blocks (e.g., from Figure 5B to Figure 5C) results in a model that is  
476 better conditioned for the inversion procedure because there are fewer model parameters to be  
477 constrained by the available geodetic data. The procedure ensures that the important parameters,  
478 i.e., slip on real geologic faults in the database, are preserved. After a round of block number  
479 reductions, the process is repeated until the number of blocks is small enough (less than 50  
480 blocks), the number of blocks does not change, or the algorithm fails by generating a block  
481 model that is invalid. The most common reason a model becomes invalid is when the combined  
482 block is not correctly parameterized with an ordered sequence of nodes shared with an adjacent  
483 block. This condition can arise (rarely) owing to errors during the combination operation.  
484 Because of the large number of models generated, loss of a few owing to block combination

485 errors is acceptable.



486

487 **Figure 5.** A) Faults of the southern Walker Lane in the NSHM database (blue), other Quaternary faults  
488 and CA/NV state line in gray. B) Initial Delaunay triangulation of nodes that represents primitive block  
489 model, C) blocks after reduction of number of blocks through iterative combination of neighboring  
490 blocks, D) solution for block motion from this model. Color indicates vertical axis spin rate component  
491 of the solution Euler pole for each block. Block movement is massively exaggerated to illustrate sense of  
492 relative motion, and strain accumulation at block boundaries is removed to emphasis rigid long-term  
493 component of motion.

494

495

496

497 Our strategy for increasing robustness in the slip rate estimates is to generate many models to  
498 reduce dependence on any single model's representation of the fault network. While the  
499 generation of each model is deterministic (the same fault inputs will always result in the same  
500 block model geometries), small changes in the location of the bounding box with respect to the  
501 faults result in a different initial node configuration and Delaunay triangulation. All models have  
502 block boundaries that coincide with the input faults, but the other off-fault block boundaries  
503 traverse the area between the faults in different places. We generate a grid of overlapping  
504 rectangular model sub-domains with a spacing of  $0.25^\circ \times 0.25^\circ$ . At each iteration the subdomain  
505 boundary is shifted by  $0.25^\circ$  which changes the relative position between the rectangular  
506 boundary and the nodes along faults inside, resulting in a different triangulation. The grid  
507 extends beyond the area of interest (Figure 1), but if the intersection between a sub-domain and  
508 the full model domain (Figure 1) is  $<10\%$  of the sub-domain area then the model is not used. A  
509 total of 1240 block models are built using the generative procedure described above and 1231 of  
510 them (99%) were valid and could be used to estimate slip rates from the GPS velocity field.

511

### 512 3.3.3. Solving for slip rates

513 For each block model we estimate the slip rates on each fault segment using the method of  
514 Hammond et al., (2011), which assumes the geodetic data are collected during the interseismic  
515 time when the faults are locked at the surface but the block motions continue. This method is  
516 like others (e.g., McCaffrey, 2002; Meade and Hager, 2005) but uses a damped linear least  
517 squares inversion to solve simultaneously for a set of block rotations and fault slip rates. The  
518 motion of each block  $j$  is parameterized with an  $3 \times 1$  Euler rotation vector ( $\vec{\omega}_j$ ) and each fault slip

519 rate with parameters representing strike-slip ( $a_k$ ) and dip-slip ( $b_k$ ) rates for fault  $k$ . These  
 520 unknown parameters are related to the horizontal vector GPS velocity data  $\vec{v}_{GPS,i}$  at station  $i$   
 521 through the equation:

$$522 \quad \vec{v}_{GPS,i} = \vec{\omega}_j \times \vec{r}_i - \sum_{k=1}^L (a_k \mathbf{G}_{ss,ki} - b_k \mathbf{G}_{n,ki}) \quad (1)$$

523 where the first term on the right side is the contribution from block rotation at the station location  
 524  $\vec{r}_i$ , and the second term accounts for elastic strain accumulation owing to shallow locking of the  
 525 faults. The functions  $\mathbf{G}_{ss,ki}$  for strike slip and  $\mathbf{G}_{n,ki}$  for normal/thrust slip are the Green's functions  
 526 that enforce back-slip (Savage , 1988) and are calculated using functions from Okada (1985),  
 527 which are fixed by the known location of the faults and stations. Multiple faults may contribute  
 528 to elastic strain accumulation at a single station, up to a maximum of  $L$  faults, which we set in  
 529 this analysis to 6 since greater values do not change the result significantly.

530 Regularization is implemented by minimization of both fault slip and the vertical axis  
 531 spin rates. These conditions are expressed as:

$$532 \quad a_k = 0, \quad (2a)$$

$$533 \quad b_k = 0, \quad (2b)$$

$$534 \quad \vec{\omega}_j \cdot \vec{r}_j = 0, \quad (2c)$$

535 which are equations added to the system for all  $k$  and  $j$ . Adding the constraints in (2) to the  
 536 inversion problem enforces minimization of the slip and rotation rates while also fitting the data.  
 537 The weight of the damping condition is controlled by the regularization values that are a function  
 538 of background strain rate and style. This is needed because of the orders of magnitude variation  
 539 in strain rate in different locations in the Walker Lane makes spatially constant factors  
 540 ineffective in some areas. Strike slip and normal/thrust components have damping weighted  
 541 separately so that slip rates are consistent with the tensor strain rate style. The regularization

542 method is discussed in detail in the Supplemental Materials. In accordance with previous studies  
543 of the WL seismogenic depth (e.g., Zuza and Cao, 2020; Ruhl et al., 2021), in each model we  
544 assume 15 km locking depth throughout the entire area. No parameters for long term strain rates  
545 within individual blocks are included.

546

547 The median slip rates for each fault from the set of all block models is shown in Figure 6 and are  
548 provided in Supplemental Table S2. Taking the median value reduces the impact of outliers that  
549 can be seen in solutions of some individual block models (e.g., Figure 5B). Each fault has  
550 multiple segments with some variability along strike so we consider each segment as an  
551 individual sample of the slip rate which contributes to the distribution. Faults with a strike slip  
552 component have a median number of 454 individual segments contributing to the slip rate  
553 estimate (over all models and segments), but as few as 12 and as many as 3036. Long faults tend  
554 to have more individual segments, and faults near the boundary have fewer since not as many  
555 block model sub-domains cover them. There are fewer dip slip rates estimated because we did  
556 not estimate them for faults which are deemed to be vertical strike slip faults in the NSHM  
557 database. Some block models produce a slip rate that is inconsistent with the geologically  
558 determined sense of slip for the fault. We truncate the distributions of slip rates in all cases  
559 where the slip rate has a sign that is in direct conflict with the geological characterization of the  
560 fault rake and determine the median rates from the remaining distribution. East of the WL, in the  
561 Basin and Range, most of the faults were designated as normal faults in the NSHM database, so  
562 had no strike slip rate estimated. However, the normal rates were estimated and had diversity that  
563 is not possible to appreciate given the -1 to 1 mm/yr color scale limits in Figure 6. To see the

564 diversity of normal slip rates in the Basin and Range we provide another version of Figure 6B in  
565 the Supplementary Materials with color scale to -0.1 to 0.1 mm/yr (Figure S7).

## 566 **4. Results**

### 567 **4.1 Slip Rates**

568 For discussion we use the convention where dextral slip has negative and sinistral has positive  
569 sign, normal slip has negative and thrust positive rates. For a given fault we report the median  
570 slip rate for all segments and all block models that contribute an estimate. We estimate the  
571 uncertainty with the median absolute deviation (MAD) of the slip rate estimates, multiplied by  
572 1.4826 which makes the value identical to the standard deviation if the distribution of estimates  
573 is Gaussian (Wilcox, 2005). In the case of the automatically generated block models there are  
574 occasionally instances when the model returns an outlier slip rate that is not representative of the  
575 body of the distribution. Thus, using the median and MAD is advisable because they are  
576 insensitive to outliers and more representative of the body of the estimates. The resulting rates  
577 and uncertainties account for variability in fault strike and in the geometric depiction of the local  
578 block kinematics.

579 We do not divide by the square root of the number of model estimates as is done when  
580 estimating the formal uncertainty in a mean because the large number of models generated  
581 (sometimes thousands - Table S2) would make the uncertainties unrealistically small. However,  
582 faults that have high degree of strike variability or higher slip rates will tend to have larger  
583 uncertainties not because of greater error in the models, but because the geometric variability  
584 along the fault maps to variability in slip rate, or their geometries are difficult for the block  
585 generator to represent consistently. The resulting set of fault slip rates reveals the distribution of  
586 active deformation into domains in the major sub-provinces of the WL (Figure 6).

587

588 Strike slip rates are generally higher in the SWL, CWL and NWL compared to the rates in the  
589 Basin and Range east of the WL. For example, in the SWL the long northwest striking dextral  
590 faults accommodate the largest amount of deformation. The fastest dextral rate is  $-4.2 \pm 1.4$   
591 mm/yr (dextral) for the Hunter Mountain/Saline Valley Fault, followed next by  $-2.9 \pm 1.0$  mm/yr  
592 (dextral) for the Death Valley Black Mountains segment,  $-1.5 \pm 0.6$  mm/yr for the Owens Valley  
593 Fault, and  $-0.8 \pm 0.6$  for the Panamint Valley fault. These faults account for most of the velocity  
594 budget of across the SWL (Figure 2). While there is a strong contrast between high slip rates in  
595 the SWL and low rates in the Basin and Range exclusive of the WL, some SWL slip rates are  
596 low, even though they reside in areas with higher strain rates. For example, the extension rates  
597 of the Deep Springs Valley ( $-0.4 \pm 0.1$  mm/yr), Dry Mountain ( $-0.2 \pm 0.2$  mm/yr), Tin Mountain ( $-$   
598  $0.1 \pm 0.1$ ), Towne Pass ( $-0.6 \pm 0.3$ ) faults are systems that accommodate northwest-southeast  
599 oriented extension amid the ranges that lie between the Death Valley, Panamint Valley, and  
600 White Mountain fault systems.

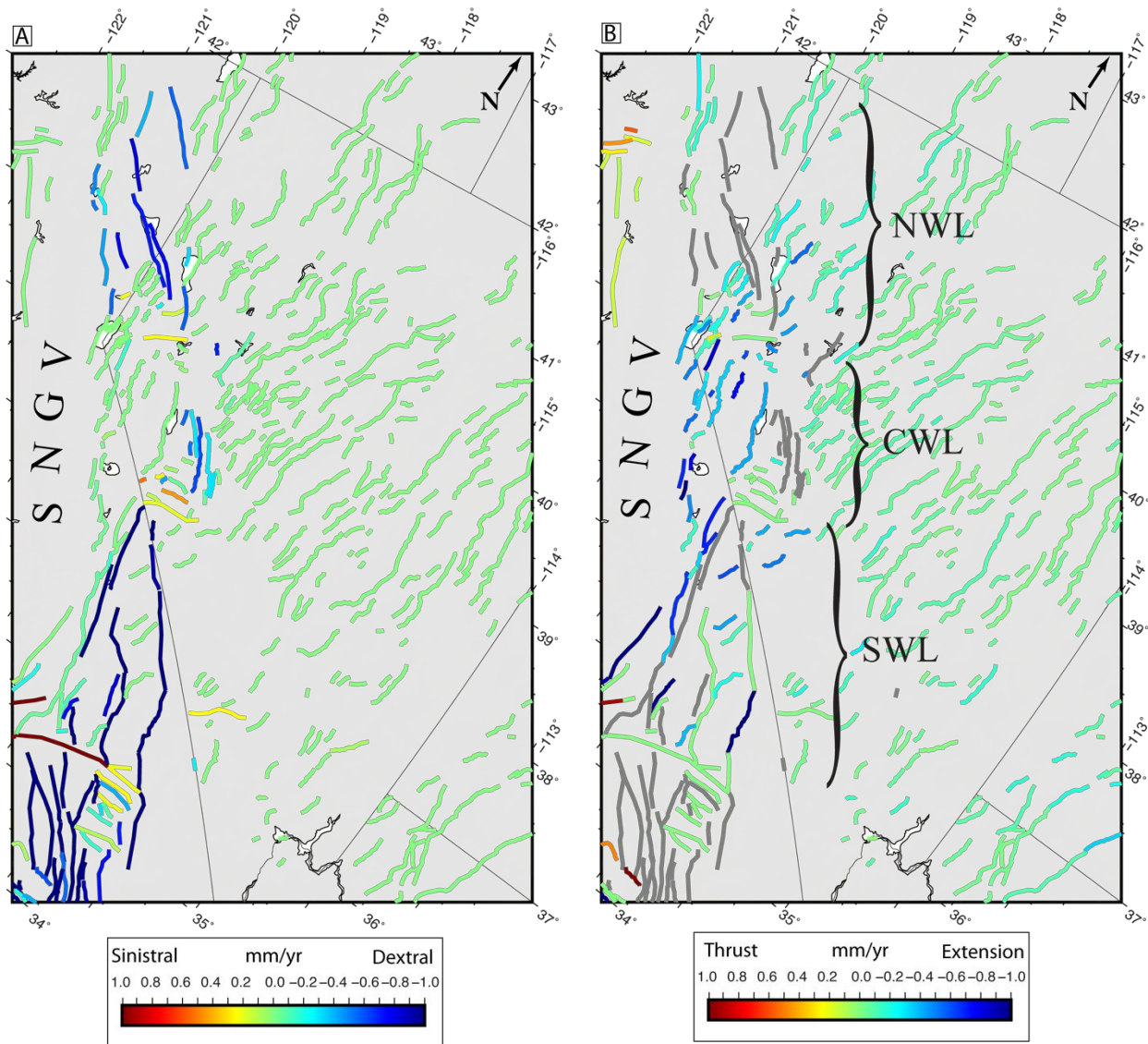
601

602 In the CWL there is evidence of partitioning, where faster strike slip rates (faster than 1 mm/yr)  
603 step right at the Mina Deflection from Fish Lake Valley and White Mountain into the Gumdrop,  
604 Benton Springs and Bettles Well/Petrified Springs fault systems east of Walker Lake. This is  
605 consistent with geological observations of fault rakes (Wesnousky, 2005; Surpless, 2008;  
606 Angster et al., 2019; Pierce et al., 2021) and in our model is in part a consequence of imposing  
607 constraints on rake from the geologic database (Hatem et al., 2022a), which suppresses strike slip  
608 on faults with rake =  $-90$ . The relatively high dextral slip rates stay to the east edge of the WL

609 until further north in the NWL, north of the latitude of Lake Tahoe, they become distributed  
610 across the width of the WL between the SNGV and Pyramid Lake (Figure 6).

611

612



613  
614 **Figure 6.** A) Strike slip component of fault slip rates in the WL, B) dip slip component (projected to  
615 horizontal). Gray colored faults are those for which the NSHM database prescribed it to be a vertical  
616 strike slip fault, so no dip slip component was estimated. SNGV is the Sierra Nevada/Great Valley  
617 microplate. NWL, CWL, and SWL denote Northern, Central and Southern Walker Lane. A version of B)  
618 with color scale limits narrowed to -0.1 to 0.1 mm/yr shows variability of the slow slip rates in the Basin  
619 and Range of central to eastern Nevada, is presented in the Supplementary Materials.  
620

621  
622 In the NWL the higher dextral rates associated with the WL extend at least as far north as the  
623 northern end of the SNGV microplate, including the Lake Almanor, Eagle Lake and Likely fault  
624 systems (faults names are labeled on Figure S1). We see thrust sense on faults immediately  
625 north of the SNGV microplate, where it interacts with the Klamath Mountains and Oregon  
626 Coastal microplate at the Red Bluff, Bear Creek and Inks Creek faults (Figure S1), consistent  
627 with expectation based on other geodetic, geologic, and seismic studies (Williams et al., 2006;  
628 Unruh and Humphrey, 2017; Angster et al., 2020). The rate on the Hat Creek Fault to the north is  
629 slow and mostly normal sense ( $-0.1 \pm 0.1$  mm/yr). Here, normal slip was not permitted on these  
630 faults since in the geologic database their dips were  $90^\circ$ .

631  
632 The model images sinistral slip along the east-northeast striking faults that cross the WL and  
633 reach to its eastern edge such as the faults of the Mina Deflection, Garlock and Olinghouse  
634 faults, and Carson lineament. Sinistral slip on these structures is consistent with median model  
635 clockwise vertical axis rotations that are discussed below, with expectation based on models of  
636 blocks rotating in northwest directed shear field (McKenzie and Jackson, 1983; Platt and Becker,  
637 2013; Bormann et al., 2016; deLano et al., 2019), and with observations of paleomagnetic  
638 clockwise rotation (Cashman and Fontaine, 2000; Petronis et al., 2009; Carlson et al., 2013).  
639 Sinistral slip is seen at the southern end of the SNGV at the White Wolf ( $4.2 \pm 1.2$ ) and Garlock  
640 Faults (0.3 to 1.2 mm/yr increasing to the west). The Garlock fault slip rates are slower than  
641 those estimated in most geologic studies, 2.7 to 5.3 mm/yr or higher, see Hatem and Dolan,  
642 (2018) and references therein for a summary. We include only its central and easternmost

643 segments here, which are slower than its western section, in both this study and in geologic  
644 observations (McGill et al., 2009).

645

646 Normal slip rates in the WL are also generally higher than normal slip rates in the Basin and  
647 Range to the east, which are all closer to zero than  $-0.2$  mm/yr. While the WL strain rate field is  
648 dominated by shear, it also has enough positive dilatation and releasing bends in the fault  
649 systems to drive normal slip. Some long faults have relatively fast normal slip rates with  
650 uncertainties  $0.5$  mm/yr or less (e.g., northern Kern Canyon  $-1.4 \pm 0.5$  mm/yr). The very highest  
651 normal slip rates are on shorter faults that tend to have high uncertainties (e.g., Hartley Springs at  
652  $-1.8 \pm 1.5$  and Airport Lake  $-1.3 \pm 1.0$  mm/yr). These are both in locations with multiple  
653 intersecting or near-overlapping faults, so the block construction algorithm may be drawing  
654 boundaries around these faults in a greater variety of ways. Extension occurs on most faults  
655 north of the Garlock if they do not dip  $90^\circ$  in the fault database, on which normal slip was not  
656 estimated (gray faults in Figure 6B). In the CWL normal slip is distributed between Lake Tahoe  
657 and the Wassuk Fault near Walker Lake. In the area northwest of Lake Tahoe, between the  
658 Mohawk Valley Fault and Pyramid Lake has positive dilatation, but the faults in the NSHM  
659 database are all vertical strike slip faults, so normal slip was not estimated.

660 Normal slip on the Lone Mountain ( $0.6 \pm 0.4$  mm/yr), Clayton Valley ( $0.5 \pm 0.4$  mm/yr) and  
661 Emigrant Peak ( $0.4 \pm 0.3$  mm/yr) faults, south of the Mina Deflection and east of the WL show  
662 extension across the Silver Peak/Lone Mountain complex and appear consistent with  
663 displacement-transfer style faulting (Oldow, 1992; Oldow 1994) and geological fault slip rates to  
664 within uncertainty (Foy et al., 2012; Lifton et al., 2015).

665

666 In the Basin and Range east of the WL the median normal slip rate is -0.05 mm/yr and robust  
667 measure of their standard deviation is 0.05 mm/yr. This suggests that the geodetically measured  
668 deformation observed across the eastern Nevada Basin and Range (Hammond et al., 2014) is  
669 discernable in the slip rates. It is also consistent with the strain release rate observed in  
670 paleoseismic trenches on the active normal fault systems between 38.5° and 40.0° that  
671 cumulatively add to between 0.8 to 1.0 mm/yr of extension across 450 km (Koehler and  
672 Wesnousky, 2011). If ranges are separated by ~30 km then 450 km equates to 15 ranges or 0.07  
673 mm/yr extension per range, similar to our median geodetic normal slip rate.

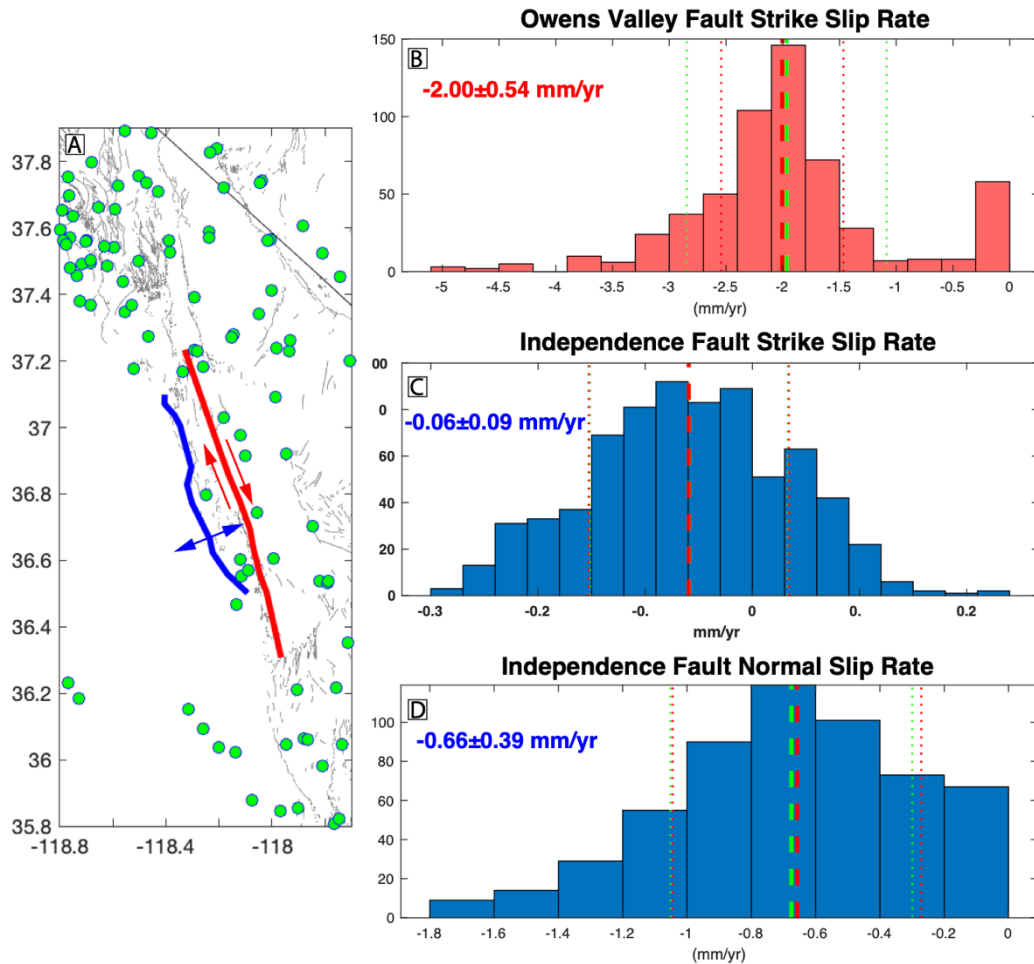
674

675 While Hammond et al., (2014) found a shear sense of strain rate in the geodetic data, there is no  
676 systematic strike slip component in the slip rates estimated here or in the trenches of Koehler and  
677 Wesnousky (2011). While the signal of extension is clear in the normal slip rates, there is a  
678 possibility that our regularization based on scaling by our GPS strain rates model could be  
679 suppressing the signal of strike slip since the strain rate in eastern Nevada is very low ( $<5 \times 10^{-9}$   
680  $\text{yr}^{-1}$ ). Another possibility is that the shear observed in geodesy is a transient deformation  
681 associated with the sum of many past and possibly distant western US earthquakes. This is  
682 predicted by the forward model of Young et al., (2023) at a level below  $2 \times 10^{-9} \text{yr}^{-1}$ . Removing  
683 their predicted postseismic strain from the observed strain rate makes it more uniaxial with an  
684 east west extension direction similar to the geologic extension direction. Whether transients are  
685 affecting the GB in this way deserves more direct study of the potentially far-reaching impact of  
686 post-earthquake viscoelastic transients.

687

## 688 **4.2 Slip Partitioning**

689 We provide an example that shows the effectiveness of the method and regularization in  
690 partitioning transtensional strain appropriately between closely adjacent strike slip and normal  
691 faults. The Owens Valley fault is a vertical strike slip fault and is closely adjacent to (3-15 km)  
692 the Independence Fault which is an east dipping normal fault that bounds the Sierra Nevada  
693 range front (Figure 7). Their proximity means that the motion of the area between them must be  
694 constrained in a robust way to accurately estimate both slip rates in a block model. Adding to  
695 the challenge is the asymmetry in the strength of GPS data coverage, with strong network  
696 coverage in the SWL to the east and weak coverage in the Sierra Nevada wilderness areas to the  
697 west. Our method finds a strike slip rate for Owens Valley of  $-1.5 \pm 0.6$  mm/yr (dextral) and for  
698 the Independence Fault  $-0.1 \pm 0.1$  mm/yr for its strike slip rate and  $-0.5 \pm 0.30$  mm/yr normal slip  
699 rate. These rates are in accordance with geologic observations in terms of rates and style  
700 (Beanland and Clark, 1994; Lee et al., 2001; Bacon and Pezzonpane, 2007; Jayko et al., 2009;  
701 Haddon et al., 2016). While the normal component of slip on the Independence Fault is only  
702 significant at the 1-sigma level, the higher level of uncertainty is to be expected here because of  
703 the lack of GPS constraint west of the fault and the variability of its strike. This example  
704 suggests that the combined power of the features of the method results in robust estimates of  
705 fault slip rates that abide by geologic constraints, provide realistic uncertainties, without  
706 explicitly constraining the rates to geologically determined rates a priori.  
707



708

709 **Figure 7.** A) Owens Valley (red) and Independence (blue) Faults. Green circles are locations of nearby  
 710 GPS stations, gray lines are Quaternary faults. B) Histogram of estimates of strike slip rate for Owens  
 711 Valley Fault. No normal rate was estimated since it is categorized as a vertical strike slip fault in the  
 712 geologic database. The green/red dashed vertical lines indicate the mean/median values in the  
 713 distribution respectively. The Independence Fault strike slip rates are shown in C) normal component  
 714 rates are shown in D). In B, C and D the green/red dotted vertical lines are  $\pm 1$  standard deviation from the  
 715 mean and  $\pm 1.4826$  times the median absolute deviation from the median respectively.  
 716

### 717 4.3 Vertical Axis Block Rotations

718 Rigid block motion on the surface of a sphere can be decomposed into two orthogonal  
 719 components. The first is translation of the block associated with an Euler rotation vector  $90^\circ$   
 720 distant from the block centroid, the second is vertical axis spin which is associated with an Euler  
 721 rotation vector parallel to the direction pointing to the block centroid from Earth center. For

722 each block we separate its estimated Euler rotation vector into these two components and then  
723 using the vertical axis spin component estimate at each pixel on the map the median spin rate  
724 from all the models (Figure 8).

725

726 The resulting image shows that in the WL spin is mostly clockwise with values less than  $2^\circ/\text{My}$ .

727 Pockets of faster spin rates occur near the locations of east-northeast sinistral faults, including  
728 the Mina Deflection, Olinghouse Fault, Carson lineament, Garlock Fault and faults south of it.

729 The association between sinistral faulting and clockwise rotation is consistent with the  
730 paleomagnetic data and models of rotations as noted in the previous section. There is also  
731 clockwise rotation in the CWL west of the Wassuk Range Fault and east of Smith Valley of  
732  $\sim 1^\circ/\text{My}$  consistent with other recent CWL block models (Bormann et al., 2016).

733

734 Even greater degrees of vertical axis spin rate are seen north of the SNGV. However, in this area  
735 the geographic density of faults in the NSHM sources database is very low. For example, there is  
736 an usually large gap between the Pongosa proxy fault and the next fault to the west which is the  
737 Trinidad Fault near the California coast 200 km west (off of map in Figure S1). Thus, clockwise  
738 spin is needed to accommodate GPS velocity gradients that are part of the regional clockwise  
739 rotation pattern between the SNGV and Oregon Coast microplate (Hammond and Thatcher,  
740 2005; Williams et al, 2006; Unruh and Humphrey, 2017). Also, there is an unusually large gap of  
741 74 km between the active Surprise/Warner Valley faults and Steens Mountain fault systems  
742 (Personius et al., 2007; 2009) in which there is no fault in the sources database, though dozens of  
743 shorter faults are present in the USGS QFFD (USGS and AGS, 2011; USGS and CGS, 2011;  
744 USGS and NBMG, 2011; USGS and UGS, 2011). Here there are moderate clockwise rotation

745 rates in our model (-0.5 to -1.0°/Myr), possibly because of fewer faults are present in fault  
746 database so the GPS velocity gradients tend to be accommodated through block rotation rather  
747 than fault slip. If faults missing from the database are included in a future release, the rates of  
748 block vertical axis spin needed to explain the GPS data may be reduced.

749

750 Crossing southern Nevada is a zone of positive (counter-clockwise) spin that follows a band of  
751 seismicity that extends from southwest Utah to the SWL. Known as the Southern Nevada  
752 transverse zone (Slemmons et al., 1965) it has been characterized with GPS measurements as a  
753 zone of sinistral deformation transfer between the Wasatch Fault system and SWL called the  
754 Pahrnaghat Shear Zone (Kreemer et al., 2010). However, this band is in a zone where there is a  
755 low density of fault segments in the database, and so high rotation may be imaged. Also, this  
756 zone has lower GPS station density (Figure 1B), making it more difficult to resolve the zone's  
757 location precisely. It does extend all the way to the Death Valley fault, and crosses it to the  
758 Hunter Mountain/Saline Valley fault, encompassing Tin Mountain and Dry Mountain faults.

759

760

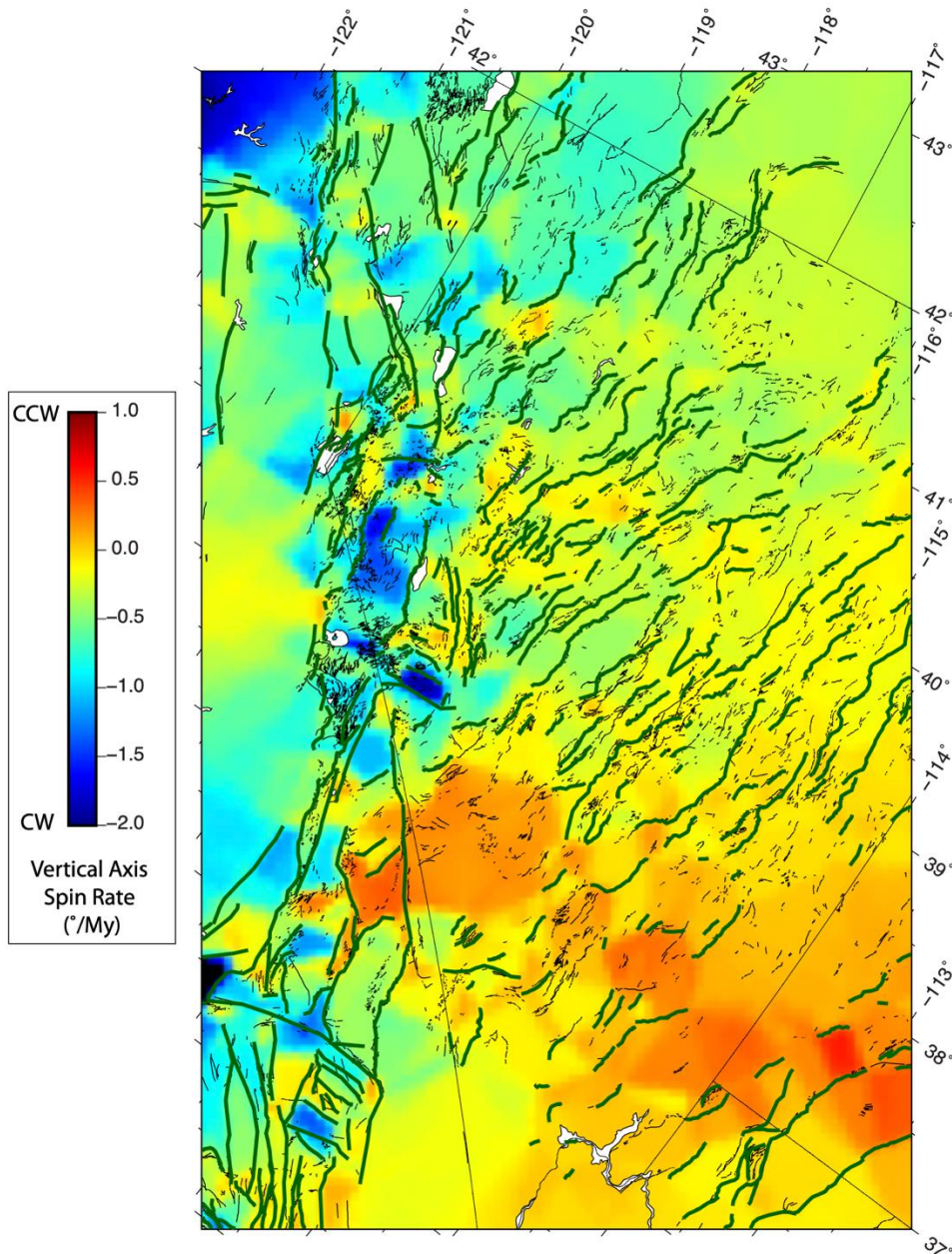
761

762

763

764

765



766

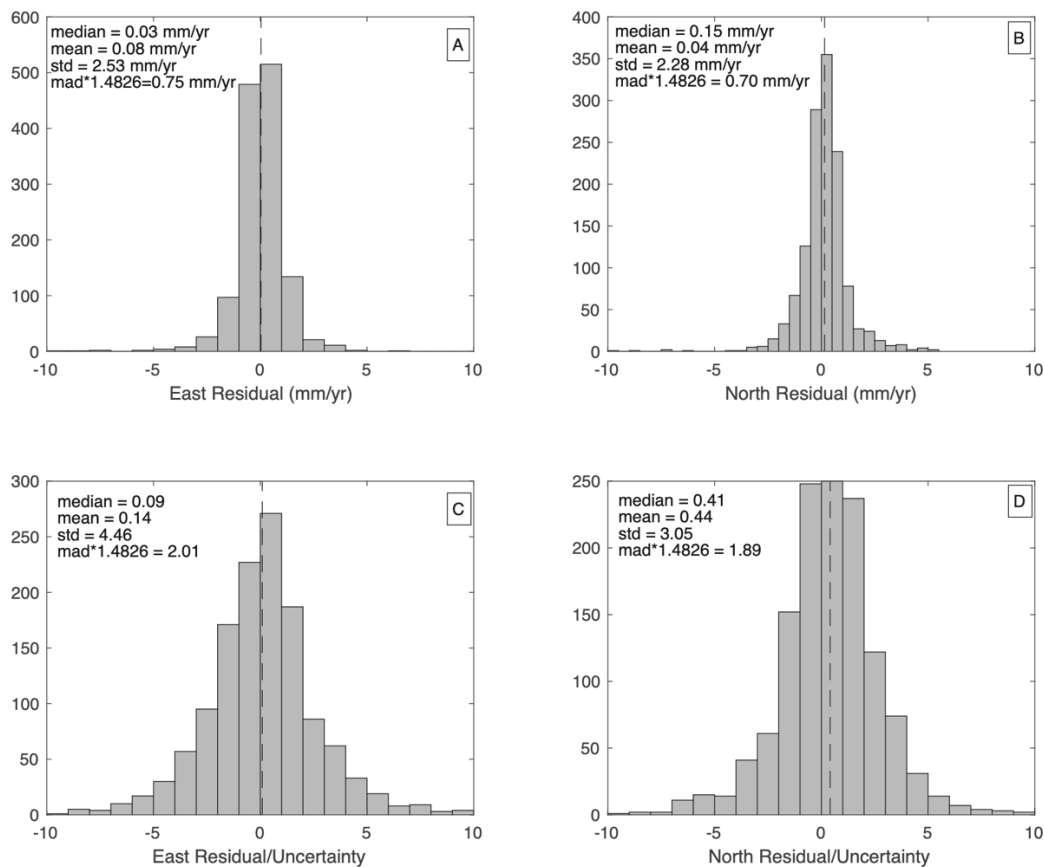
767 **Figure 8.** Image of median block vertical axis rotation rate. Color scale indicates rate and sign, positive  
 768 (red) is counter-clockwise, negative (blue) is clockwise.

769

#### 770 4.4 Model Uncertainties and Data Misfit

771 Misfit of the models to the data is obtained by finding for each GPS station the median predicted  
 772 east and north velocity from the subset of block models that use the station. The residuals are the  
 773 difference between the original GPS velocities (not the gridded or filtered velocities) and the

774 predictions (Figure 9). The figure annotation shows the median absolute deviation (MAD) times  
 775 1.4826 of residuals is significantly smaller than the standard deviation indicating that outliers  
 776 affect the standard deviations substantially (by about a factor of 3 over the robust estimate made  
 777 with the MAD). The histograms of residuals normalized by their uncertainties have  
 778  $MAD * 1.4826$  of  $\sim 2$  indicating that the data are fit at a level about twice the uncertainties in the  
 779 velocities, with a robust estimate of RMS of  $\sim 0.7$  mm/yr. Our misfit is a bit lower than those in  
 780 the NSHM western US models (Johnson et al., 2024) in part because we use the robust estimate  
 781 which reduces impact of outliers and we focus on a subset of the western US with slower  
 782 deformation.



783  
 784 **Figure 9.** Histograms of residual velocity in the east coordinate (left) and north coordinate (right). Top  
 785 row indicates residuals in mm/yr, bottom row shows residual velocity components normalized by their  
 786 individual component velocity uncertainties. See text for discussion.  
 787

788 The histograms show near zero mean for the east and north residuals, with a slight tendency for  
 789 positive mean north residual at the level of  $\sim 0.1$  mm/yr. To address the potential for systematic  
 790 misfit we use a definition of systematicity that for each station takes the mean dot product of  
 791 neighboring station velocities (defined by Johnson et al., 2024):

$$792 \quad S_i = \left( \sum_{j=1}^n \frac{\vec{v}_i \cdot \vec{v}_j}{|\vec{v}_i| |\vec{v}_j|} \right) / n \quad (3)$$

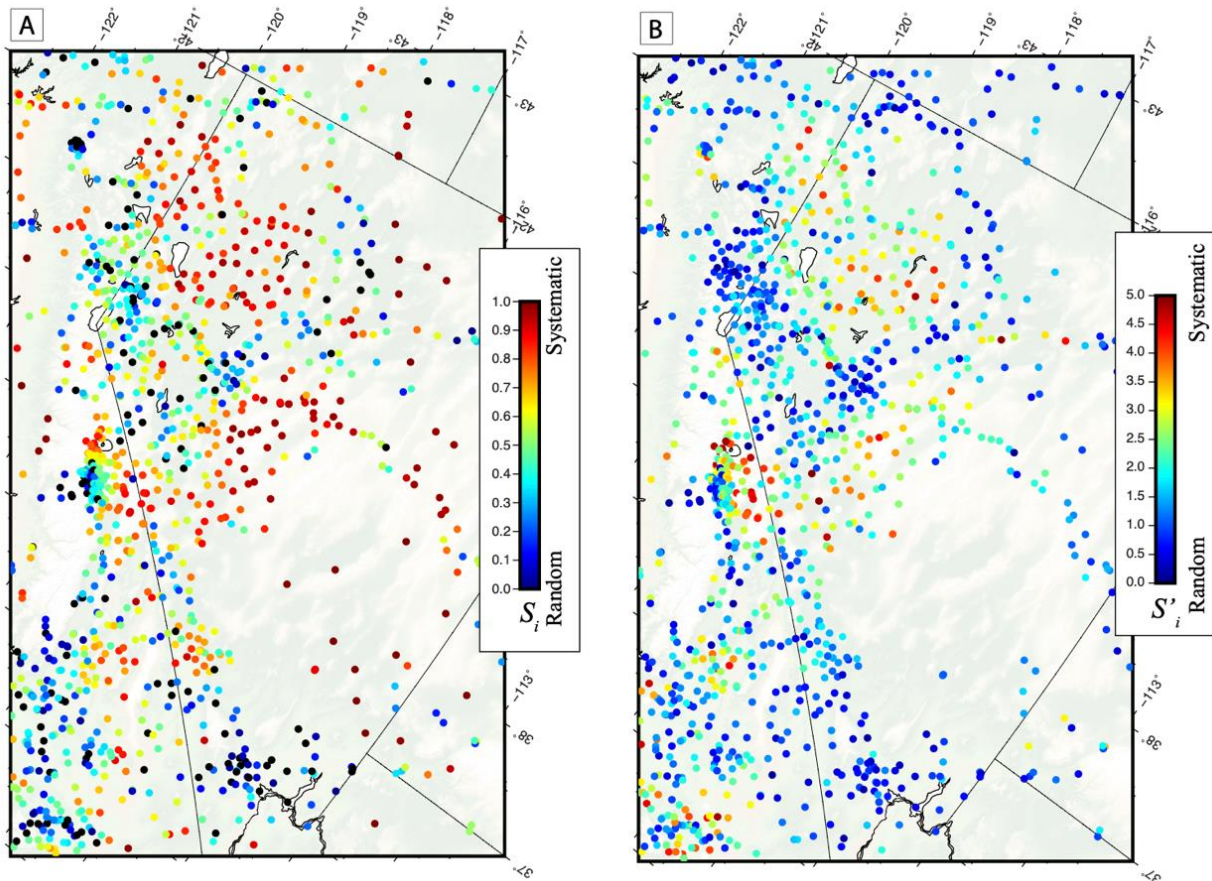
794  
 795 We use a radius of 30 km in the vicinity of each station  $i$  to select the  $n$  nearest stations. When  
 796 velocities have similar azimuths their dot products have higher magnitudes and  $S_i$  increases,  
 797 while when the vectors have random azimuths the signed dot product values tend to drive  $S_i$   
 798 towards zero. This measure varies between 0 for very randomly oriented vectors to 1 when they  
 799 all have the same azimuth. The absolute value of  $S_i$  for each station is plotted in Figure 10A, and  
 800 reveals domains with significant systematicity, similar to the models that comprise the NSHM  
 801 deformation model suite (Johnson et al., 2024). However, this measure does not consider the  
 802 uncertainties in the velocities so may give the visual impression that large areas have systematic  
 803 residuals, even if the residual velocity magnitudes are below the uncertainties in the data.

804  
 805 To address this we define an alternative version of the formula that normalizes the residual  
 806 vectors by their uncertainties instead of the residual norms:

$$807 \quad S'_i = \left( \sum_{j=1}^n \sqrt{\frac{\vec{v}_i \cdot \vec{v}_j}{\sigma_{\vec{v}_i} \sigma_{\vec{v}_j}}} \right) / n \quad (4)$$

809

810 When we look at Figure 10B which is based on equation (4) we see that many of the residuals  
811 that were highly systematic in Figure 10A have residuals that are well below the uncertainties in  
812 the velocity data. This is expected because these small residuals will not influence the least  
813 squares inversions for block rotation and slip rate parameters as much as other more significant  
814 residuals. There are, however, still a few significant systematic residuals in the vicinity of Long  
815 Valley Caldera where magmatic inflation drives radial signals that are not well modeled on the  
816 CWL fault systems. Also, in the NWL near the epicenters of the 1954 Fairview Peak and Dixie  
817 Valley earthquakes, where the CNSB postseismic relaxation has been modeled and removed (see  
818 Section 3.2), we see an indication of systematic misfit with  $S' \sim 3-4$ . This suggests that the signal  
819 from CNSB postseismic relaxation may not be completely removed and some signal that is not  
820 well modeled by CNSB faults remains. The third area with high  $S'$  values is east of the dextral  
821 faults in the eastern CWL near the Toiyabe Range. This anomaly is near the source of the 1932  
822 M7.1 Cedar Mountain earthquake, which is another events included in the CNSB transient  
823 postseismic relaxation model and so may also be indicating that the transient signal is not  
824 entirely removed.



825

826 **Figure 10.** A) Systematicity of residual values  $S_i$ . Color scale shows blue for randomly oriented residuals  
 827 and red is for neighboring stations with very similar residual azimuth. B) is systematicity  $S'_i$  which  
 828 normalizes the residual vectors by velocity uncertainty rather than residual vector magnitude. Both  
 829 measures are unitless. When normalizing using velocity uncertainties the zones of systematic misfit are  
 830 less extensive and occur areas with significant time-variable deformation.

831

## 832 5. Discussion

### 833 5.1 Comparisons between geologic and geodetic slip rates

834 Geologic and geodetic slip rates each aim to measure the same thing, i.e., the relative rate of  
 835 motion of blocks of Earth's crust on either side of a fault. However, they use very different  
 836 means to measure displacement over very different time scales. Geologic data constrain relative  
 837 motion across faults and in landscapes over the long periods of time needed to accumulate  
 838 measurable displacements of earth materials. Geodetic data, because of their high precision can

839 constrain displacements over a few years to decades (Bennett, 2007). Similarity between  
840 geologic and geodetic slip rates indicates that the different methods are estimating the same  
841 potential for slip at different times in the earthquake cycle, which increases confidence in the  
842 results. Because strain rates in the WL are slower than along the main plate boundary fault zones  
843 in western California, our slip rates occupy a much slower and narrower range than in other  
844 recent comparisons. It is therefore more challenging to establish a correlation between geodetic  
845 and geologic rates in the WL. It is important to note that unlike in some other studies (e.g.,  
846 Pollitz, 2022; Zeng, 2022; Shen and Bird, 2022) we do not use geologic slip rates as prior  
847 constraints or bounds on the solution for slip. Thus, our geodetic rates have a higher degree of  
848 independence from the geologic rates and are corroborative of them when they agree.

849

850 We compare our geodetic slip rates to geologic rates from a recent compilation developed to  
851 support the NSHM (Hatem et al., 2022b, which we also provide in Table S2). We exclude faults  
852 south of 34.8° latitude and the Garlock fault because its geologic rate in the NSHM database (up  
853 to 11 mm/yr) is much greater than the range of all other faults in this study and our estimate (1.2  
854 mm/yr in the central section). The result (Figure 11A) shows a degree of agreement but many  
855 slip rates are less than 1 mm/yr so we also plot them on a  $\log_{10}$  axes (Figure 11B). The log scale  
856 plot reveals a general trend of agreement between the geodetic and geologic slip rates. The  
857 correlation between slip rates is similar on linear ( $r=0.37$ ) and  $\log_{10}$  scales ( $r=0.44$ ). This is a  
858 weaker correlation compared to rates across the entire Western US, which are between 0.41 and  
859 0.88 depending on the contributing modeler (Johnson et al., 2024). However, a lower correlation  
860 is expected given the far narrower range of slip rates in the WL (all are less than 5 mm/yr), and  
861 because we do not impose a constraint in our modeling that our slip rates should be near the

862 geologic rates. Nonetheless our conclusions are similar to what was observed for the entire  
863 western US: that the faults with the lowest geologic rates ( $<0.05$  mm/yr) have higher geodetic  
864 rates (Figure 11B). If we reckon that slip rates agree when the geodetic rates are within the  
865 geologic minimum/maximum bounds or when the geologic rates are within 2 times the geodetic  
866 uncertainties (to be within their 95% confidence interval), then 70 out of 362 slip rates (19.3%)  
867 disagree and the rest (80.7%) agree.

868

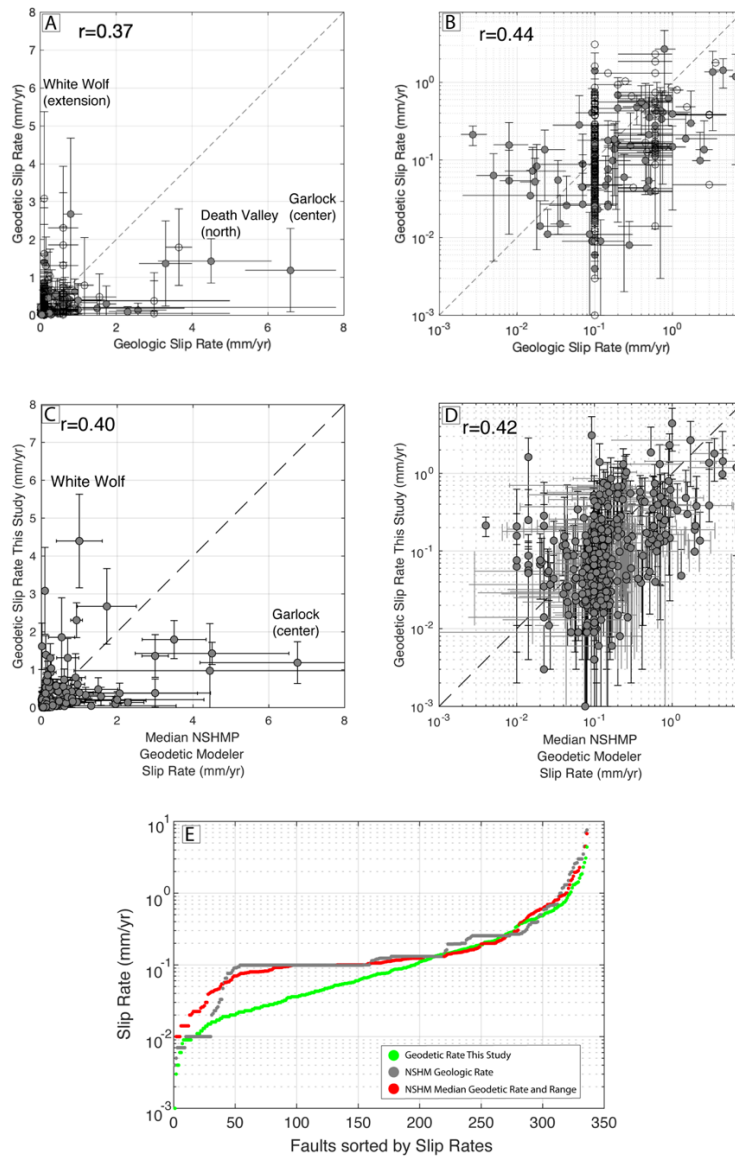
869 We also compare our geodetic rates to the median geodetic rates from the western US geodetic  
870 modelers (Figure 11C and D). The correlations are slightly higher than the correlation with the  
871 geologic rates, with  $r=0.40$  for linear scale and  $r=0.42$  for  $\log_{10}$  scale. Because we solve for the  
872 same parameters from the same data, we may expect some agreement with their results.

873 However, many of the NSHM modelers optimized their analyses for 1) a much larger and more  
874 tectonically diverse area with slip rates that vary by several orders of magnitude, 2) used a  
875 variety of analytical techniques, and 3) used geologic rates as prior constraints. The similarity of  
876 correlation shows that our rates agree with other geodetic slip rates about as well as they agree  
877 with geological slip rates. This may possibly be because the NSHM modelers relied heavily on  
878 geologic rates.

879

880 In the GB east of the WL, many of the faults have low slip rates, both in our model and in the  
881 NSHM database. In this area many geologic rates in the NSHM database have slip rates exactly  
882  $0.1$  mm/yr because they had no preferred rate, only a minimum of  $0.0$  mm/yr and maximum of  
883  $0.2$  mm/yr. In these cases, we took the geologic rate to be the mean of the minimum and  
884 maximum (Figure 11B). Our geodetic rates for these faults vary between  $<0.01$  mm/yr to over 1

885 mm/yr. The median difference between geologic and geodetic rates in this area is 0.03 mm/yr  
886 which is close enough to zero to indicate that there is no bias for geologic or geodetic rates being  
887 greater. The median absolute deviation of the differences is 0.10 mm/yr. The absolute level of  
888 disagreement is very small mostly because there are so many faults in the Basin and Range with  
889 very low slip rates, and any slip rate estimate consistent with the low background strain rate  
890 would be similar at the level of 0.1 mm/yr. It is an advantage of our robust multi-block method  
891 that it returns the geologically plausible slip rates for large areas of the GB with many low slip  
892 rate faults.



893  
894  
895  
896  
897  
898  
899  
900  
901  
902  
903  
904  
905  
906

**Figure 11.** Comparison of geodetic slip rates from this study to A) slip rates from the geologic slip rate database (Hatem et al., 2022b) excluding the Garlock Fault, B) same as A) except with  $\log_{10}$  scale axes. The horizontal error bar gives the range of low to high geologic rate. If there is a preferred geologic rate it is plotted with a gray-filled circle, else an open circle is plotted at the mean between the low and high rates. Middle row shows comparison of geodetic slip rates from this study to C) geodetic slip rates from the NSHM geodetic deformation modelers as tabulated by Johnson et al., (2024). D) is same but on  $\log_{10}$  scaled axes. On all plots the vertical error bars are 2 times the uncertainty in our geodetic slip rates. E) shows the geodetic slip rates from this study (green circles), NSHM geodetic rates (red circles), and NSHM geologic rates (gray circles) sorted by slip rate. These curves show the similarity in distribution of the NSHM geologic and NSHM geodetic rates, and more continuous variation of slip rates from this study. Faults with the greatest disagreement between geologic, our geodetic, and NSHM geodetic are annotated in A) and C).

907 Lastly, in Figure 11E we compare the distributions of NSHM geologic and NSHM geodetic slip  
908 rates to our geodetic rates. The faults in each set are sorted from smallest to largest slip rate value  
909 and plotted in order. While it is difficult to show that our slip rates have greater accuracy  
910 compared to the true slip rates, the distribution shows that they have a more natural diversity in  
911 slip rate estimates especially below, and without clustering at 0.1 mm/yr. The similarity in  
912 distribution between the NSHM geodetic and NSHM geologic slip rates is likely a symptom of  
913 the dependence of NSHM geodetic rates on NSHM geologic rates. This may lead to a systematic  
914 overestimation of integrated moment in the Basin and Range if the 0.1 mm/yr value is used for  
915 all faults.

916

## 917 **5.2 Off-Fault Deformation**

918 Wesnousky et al., (2012) showed that there are paths that can be walked from the Sierra Nevada  
919 crest across the CWL that do not cross a mapped fault, suggesting that in some locations the  
920 relative motion between the SNGV and GB is accommodated without faulting. Moreover, the  
921 geodetic modelers for the western US NSHM explicitly quantified deformation in the GPS data  
922 that was not mapped onto faults and derived off-fault moment rates between 31 and 58% across  
923 the Western US. Off-fault deformation may represent strain in the deformation budget that  
924 occurs near, but not on the main fault strands (Oskin et al., 2007; McGill et al., 2015), or  
925 possibility entire crustal blocks undergo non-brittle deformation by developing folds or oroclinal  
926 flexures that accommodate strain (e.g., Faulds and Henry, 2008), or some other process.

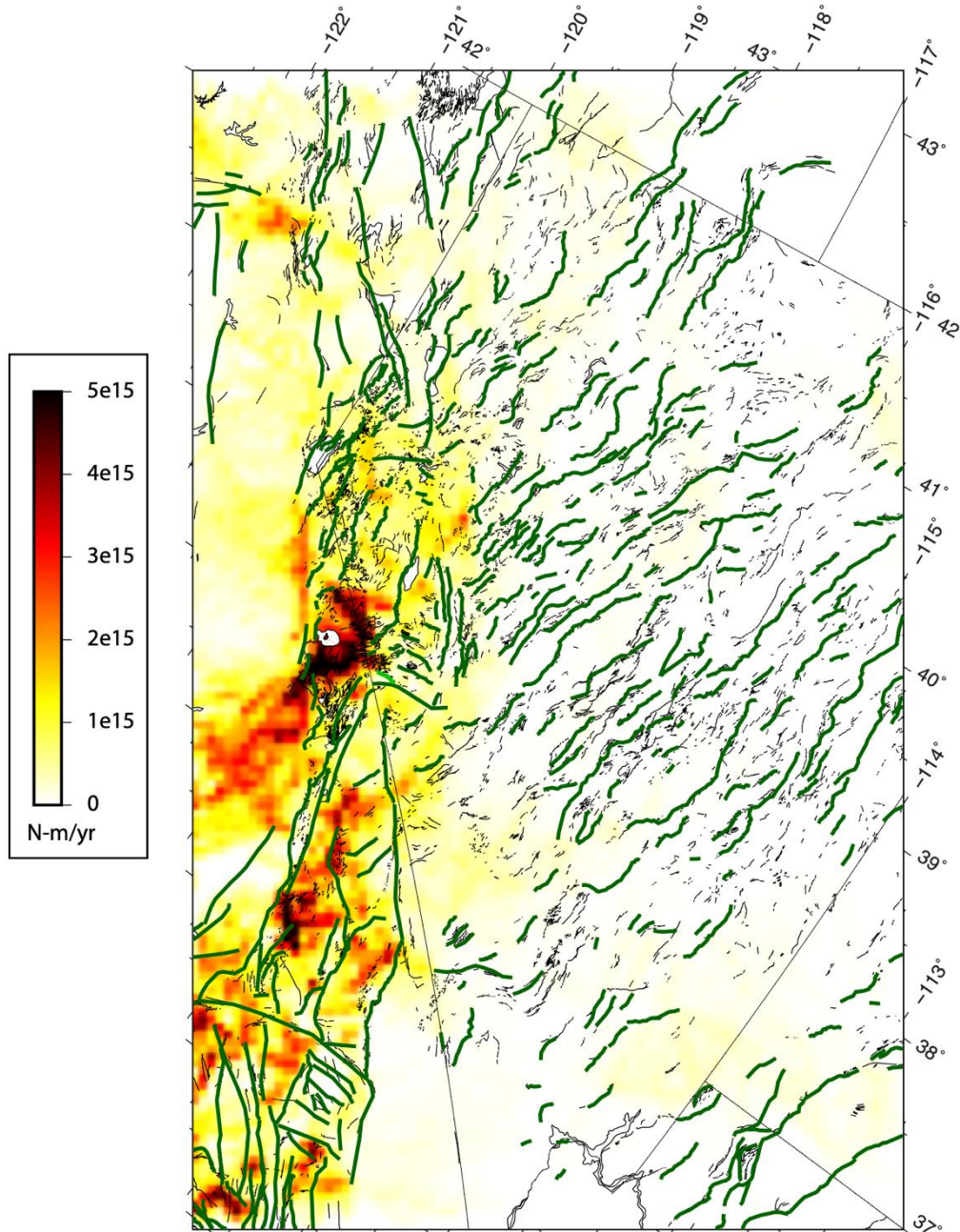
927

928 We estimate on-fault deformation as moment from slip on the active faults in the NSHM sources  
929 database. We sum the moments by assuming a constant seismogenic thickness of  $H=15$  km, a

930 shear modulus of  $G=30$  GPa, and use fault areas of the locked segments  $A = LW$ , where  $W =$   
931  $H/\sin(\text{dip})$  and  $L$  is fault length. Summing over all faults segments the quantity  $GHAs$ , where  $s$   
932 is the slip rate gives a total on-fault moment of  $4.3 \times 10^{18}$  N-m in our model domain. We  
933 estimate off-fault deformation by summing the same terms over all the boundaries between  
934 blocks that are not in the NSHM database. The block boundaries are not guaranteed to occur in  
935 the same place in every iteration or to have the same sign of slip. Thus, the off-fault moment is  
936 distributed within zones between the NSHM model faults (Figure 12). The total off-fault  
937 moment rate in the domain is  $9.1 \times 10^{18}$  N-m, giving an off-fault deformation proportion of 68%.  
938  
939 This proportion of off-fault deformation is higher than that found in western US models for the  
940 NSHM (Pollitz, 2022a; Evans, 2022; Shen and Bird, 2022; Zeng, 2022a). There are two reasons  
941 why the proportion may be particularly high in the WL. First, we include explicit  
942 parameterization for off-fault deformation to occur, i.e., on block boundaries that are not faults,  
943 and this allows the deformation to be detected and quantified. While the method allows more  
944 off-fault deformation to emerge, there is a limit to how well its location is imaged, since it is  
945 forced to lie where block boundaries not in the fault database are created by the automated block  
946 generation procedure. Second, in the WL and GB there are likely more faults undiscovered  
947 and/or not included in the NSHM database, even though they are active and contribute to the  
948 accommodation of far field budgets. Many faults in the USGS QFFD (USGS and AGS, 2011;  
949 USGS and CGS, 2022; USGS and NBMG, 2011; USGS and UGS, 2011) are not present in the  
950 NSHM database (Figure 12). Thus, the degree of completeness of the fault database may be  
951 lower in the WL and GB compared to other systems in the western US, e.g., the San Andreas. A

952 recent example is the 2020 M6.5 Monte Cristo Range earthquake in Nevada which ruptured the  
953 surface on unmapped segments of the Candelaria Fault (Koehler et al., 2021).

954



955

956 **Figure 12.** Map of off-fault deformation rate. Dark green lines are faults from the NSHM database  
957 (Hatem et al., 2022a), other thin black lines are other faults in the USGS QFFD (USGS and AGS, 2011;  
958 USGS and CGS, 2022; USGS and NBMG, 2011; USGS and UGS, 2011).

959  
960 The map of off-fault deformation (Figure 12) shows that there are higher levels in areas with  
961 high strain rates, e.g., in the SWL and ECSZ. Much of the imaged deformation is in zones that  
962 are affected by time-variable processes such as the Long Valley Caldera and Coso magmatic  
963 system (Wicks et al., 2001; Montgomery-Brown et al., 2015), and the southern Sierra Nevada,  
964 which experiences hydrological loading (Hammond et al., 2016; Argus et al. 2017) and aquifer  
965 related deformation (Hammond et al., 2016; Argus et al., 2017; Neely et al., 2019). Non-tectonic  
966 processes contribute to the off-fault deformation field because they produce GPS velocity  
967 gradients that cannot be well explained as slip deficit on fault systems.

968  
969 We also see higher values where fault systems terminate and do not continue along another fault  
970 system. For example, in the SWL there is a 36 km gap between the southwest end of the Deep  
971 Springs Fault and the northern end of the Hunter Mountain/Saline Valley fault system. Here a  
972 high amount of off-fault deformation is found in our model because the block models bridge  
973 gaps with a boundary that accommodates relative motion between the NSHM faults. In east and  
974 northwest Nevada some light-yellow patches indicate deformation inside wide gaps between  
975 faults (Figure 12). Better characterizing off-fault deformation is a part of the recommendations  
976 of Johnson et al, (2024), and recognizing where the slip rate models fail to explain deformation is  
977 the beginning of better accounting for it in future models.

978

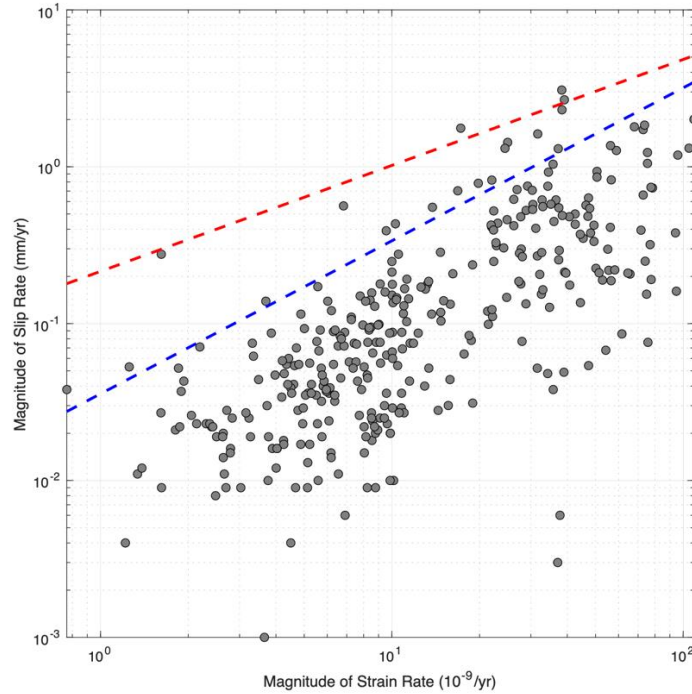
### 979 **5.3 Geodetic slip rates versus strain rate**

980 Slip rates tend to be higher in areas with higher strain rates. We can confirm that this is the case  
981 in our model by plotting the magnitude of the slip rate as a function of the magnitude of the

982 strain rate near the fault. We define magnitude of strain rate as the norm of the tensor  
983 components  $\varepsilon_{mag} = \sqrt{\varepsilon_{xx}^2 + \varepsilon_{yy}^2 + 2\varepsilon_{xy}^2}$  (Kreemer et al., 2014). We exclude faults in Long  
984 Valley Caldera because the high strain rates are from non-tectonic processes, and faults below  
985 34.8° latitude because they include the San Andreas fault which has a very high slip rate. Strain  
986 rates vary by orders of magnitude in the plate boundary, so we plot the values on a  $\log_{10}$  scale for  
987 both axes in Figure 13. The correlation between magnitudes of strain rate and slip rate is  
988 particularly strong in  $\log_{10}$  units, having  $r=0.72$  (for linear scale  $r = 0.50$ ).

989

990 If there is a strong correlation between strain rates and slip rates, this suggests that initial  
991 estimates of fault slip rates can be made directly from the strain rate maps. This approach could  
992 have utility in initializing deformation models that need prior values for slip rate inversions.  
993 These initial values would be independent of geologic slip rates, preserving the independence of  
994 the geodetic models. However, we observe that there are many cases where low slip rate faults  
995 exist in high strain rate areas. In Figure 13 there are many faults where the strain rates are over  
996  $50 \times 10^{-9}/\text{yr}$  but slip rates are below 1 mm/yr or even 0.1 mm/yr. These faults are near other  
997 faults that are doing more to accommodate the deformation budget, possibly they are more  
998 favorably located, oriented, or are more mature and mechanically efficient.



999

1000 **Figure 13.** Scatterplot of slip rate magnitude versus strain rate magnitude using  $\log_{10}$  scale for both axes.  
 1001 Strain rates at Long Valley Caldera and all faults south of  $34.7^\circ$  are excluded. Red dashed line is slip rate  
 1002 envelope based on maximum of data, blue dashed line is similar but using the 95th percentile of the slip  
 1003 rates within strain rate bins. See equations (5) and (6) for formulas.  
 1004

1005 Conversely, there are no faults in very low strain rate areas that have high slip rates (see the  
 1006 upper left corner of Figure 13). For example, when the strain rate is below  $4 \times 10^{-9}/\text{yr}$  there are  
 1007 no faults with slip rates above 0.1 mm/yr, and when strain rates are below  $10 \times 10^{-9}/\text{yr}$  there are  
 1008 no slip rates above 0.6 mm/yr. Thus, the relationship between strain rates and model slip rates  
 1009 suggests that there is an upper bound on slip rate that is a strong function of strain rate.

1010

1011 If we consider the maximum value for slip rate magnitude ( $s_{mag}$ ) inside 4 strain rate bins and use  
 1012 them to obtain an line fitting  $\log_{10}(\epsilon_{mag})$  versus  $\log_{10}(s_{mag})$  we get the red dashed line in Figure  
 1013 13. This line defines an envelope of the data above which there are almost no values for slip rate  
 1014 magnitude. The formula for the line is:

1015

1016 
$$s_{mag,max} < 0.2072 \varepsilon_{mag}^{0.7334} \quad (5)$$

1017

1018 where strain rate magnitude  $\varepsilon_{mag}$  is in units of  $10^{-9}$ /yr and slip rate magnitude  $s_{mag}$  is in mm/yr.

1019 Equation (5) gives, for example, when  $\varepsilon_{mag} = 10 \times 10^{-9}$ /yr a maximum slip rate bound of 1.12

1020 mm/yr, and when  $\varepsilon_{mag} = 100 \times 10^{-9}$  the maximum slip rate bound of 6.07 mm/yr.

1021

1022 The red line in Figure 13 describes an envelope based on maximum values of slip rates.

1023 However, it is sensitive to outliers since it is based on least squares fit to the maximum slip rates

1024 within bins. If we instead take the 95th percentile slip rate inside each of the 4 strain rate bins

1025 we get the blue dashed line in Figure 13, whose formula is:

1026

1027 
$$s_{mag,95} < 0.0347 \varepsilon_{mag}^{0.9922} \quad (6)$$

1028

1029 This gives, for example, when  $\varepsilon_{mag} = 10 \times 10^{-9}$ /yr then 95% of the slip rates will be below 0.34

1030 mm/yr, and when  $\varepsilon_{mag} = 100 \times 10^{-9}$  then 95% of the slip rates will be below 3.35 mm/yr. It

1031 may be prudent to use the 95th percentile version of the formula since its inference is less

1032 sensitive to outlier slip rates. However, it will result in fewer high slip rates which could exist if

1033 some faults slip faster than others with similar strain rates for e.g., mechanical reasons. Whether

1034 there is a similar lower bound on slip rates is equivocal since the lower right area in Figure 13

1035 has faults that slip between 0.001 to 0.1 mm/yr which are very slow and are the most difficult to

1036 resolve geodetically.

1037

1038 There are caveats. For example, the slip rates in this study were derived using a regularization  
1039 that included applying a damping of slip rates that is a function of strain rate, and so could affect  
1040 the relationships in equations (5) and (6). However, the bulk of slip rates (~80%) agree with  
1041 geological slip rates, suggesting that they are appropriately regularized. The resolution of strain  
1042 rate maps varies with technique and are sensitive to assumptions about spatial smoothing  
1043 (Supplemental text and Figure S5) and could lead to differences in results when using these  
1044 formulas. The bounding envelopes are tuned to the WL where fault density is relatively high,  
1045 but the coefficients could be customized for other regions within plate boundary zones where  
1046 strain rates are higher, more variable or fault density is lower. However, the simplicity of these  
1047 relationships suggests that when strain rate maps are available, they may be conveniently used to  
1048 generate bounding a priori values for models of slip rates on faults in complex fault zones.  
1049 Alternatively, these relations could be used as a check on models, e.g., to identify model slip  
1050 rates that are unusually large outliers in a way that does not rely on geological slip rates.

1051

## 1052 **6. Conclusions**

1053 We have presented a new method for estimating fault slip rates in areas of active tectonic  
1054 deformation that have many faults that comprise complex networks that may not completely  
1055 connect to describe contiguous blocks. The method uses an iterative algorithmically driven  
1056 construction of model block geometries to obtain many geodetic slip rates estimates for each  
1057 fault. The result obtains better sampling of the epistemic uncertainty associated with limited  
1058 knowledge of fault connectivity. The method includes constraining the models with a median  
1059 filtered and interpolated version of the GPS velocity field, applying regularization based on the  
1060 background strain rate estimated from GPS data.

1061  
1062 We applied the method to the Walker Lane in the western Great Basin to obtain a robust set of  
1063 slip rates that agree with geologic slip rates in the USGS NSHM database to within uncertainties  
1064 ~80% of the time. This is achieved without constraining the slip rates to be the same as, or in the  
1065 range of the geologic rates. We also estimated the distribution of off-fault deformation which  
1066 tends to occur in areas with higher strain rates, areas where faults in the database do not connect  
1067 end to end to other faults, and in places where non-tectonic signals are present in the GPS  
1068 velocity data.

1069  
1070 Capacity for automatic block model generation and estimating slip rates in a robust way paves  
1071 the way for larger scale application (e.g., entire Western US or world). Improving slip rate  
1072 estimates based on geodesy alone will help objectify and strengthen seismic hazards estimates in  
1073 complex fault systems.

1074

## 1075 **Open Research**

1076 RINEX data from the MAGNET GPS Network can be downloaded from  
1077 <http://geodesy.unr.edu/magnet.php>, (Blewitt et al., 2009). For stations in the NSF EarthScope  
1078 Network of the Americas (UNAVCO, 2007) data was downloaded from the GAGE facility  
1079 archive (<https://www.unavco.org/data/gps-gnss/gps-gnss.html>). Additional GPS data was  
1080 obtained from networks operated by the Arizona State Land Department, California Institute of  
1081 Technology and Jet Propulsion Laboratory (Hudnut et al., 2002), Earth System Research  
1082 Laboratory, Harvard-Smithsonian Center for Astrophysics (Wernicke et al., 2000), Hat Creek  
1083 Radio Observatory, Institute of Geophysics and Planetary Physics at U.C.S.D., Las Vegas Valley

1084 Water District, NOAA CORS Network (NGS, 1994), Pacific Northwest Geodetic Array  
1085 (PANGA, 1996), SmartNet North America, Trimble Navigation Limited, U.C. Berkeley (BARD,  
1086 2014), U.S. Coast Guard, U.S. Geological Survey (Lisowski et al., 2012), Utah Geospatial  
1087 Resource Center, and Washoe County Public Works. We used the GipsyX software and data  
1088 products including daily reference frame alignment, orbit and clock files provided by the Jet  
1089 Propulsion Laboratory (Bertiger et al., 2020). Position time series and loading corrections for  
1090 MAGNET and continuous GPS networks are freely available for download from  
1091 <http://geodesy.unr.edu>, (Blewitt et al., 2018). The predictions of non-tidal atmospheric, non-tidal  
1092 ocean, and hydrological loading use products from the European ESMGFZ ([http://rz-vm115.gfz-  
1093 potsdam.de:8080/repository](http://rz-vm115.gfz-potsdam.de:8080/repository)) (Dill and Doblsw, 2013). We incorporated additional campaign  
1094 velocity fields from GPS networks surveyed by the U.S. Geological Survey Earthquake Hazards  
1095 Program (<https://earthquake.usgs.gov/monitoring/gps>), (Murray and Svarc, 2017), and from  
1096 tables in published studies (Williams et al, 2006; McCaffrey et al., 2013; 2016; Lifton et al.,  
1097 2013; Spinler et al., 2010) including compilations (Shen et al., 2011; Kreemer et al, 2014;  
1098 Sandwell et al., 2016). Fault data was obtained from Hatem et al., (2022a) (downloaded from  
1099 <https://doi.org/10.5066/P9AU713N>) and from the USGS Quaternary Fault and Fold Database  
1100 (<https://www.usgs.gov/programs/earthquake-hazards/faults>), (USGS and AGS, 2011; USGS and  
1101 CGS, 2011; USGS and NBMG, 2011; USGS and UGS, 2011). The GPS Imaging (Hammond et  
1102 al., 2016) and block modeling software (Hammond et al., 2011) used in the analysis are publicly  
1103 available on Zenodo repositories (<https://doi.org/10.5281/zenodo.10672265> and  
1104 <https://doi.org/10.5281/zenodo.10672393>). Some figures were generated using the GMT  
1105 software version 5 (Wessel et al., 2013). For Figure 1 we used color map GMT\_seis.cpt from  
1106 cpt-city downloaded from <http://soliton.vm.bytemark.co.uk/pub/cpt-city/gmt/tn/>.

1107

## 1108 **Acknowledgements**

1109 This work would not have been possible without steadfast support from the USGS Geodetic  
1110 Networks program for data collection in the MAGNET GPS network under USGS NEHRP  
1111 projects 08HQGR0027, G13AP0018, and cooperative agreements G10AC00138, G15AC00078  
1112 and G20AC00046. Analysis was supported by USGS grant G17AP00004 and by NASA grants  
1113 80NSSC19K1044 and 80NSSC22K0463. This work is in part based on services provided by the  
1114 GAGE Facility, operated by EarthScope Consortium, with support from the National Science  
1115 Foundation, the National Aeronautics and Space Administration, and the U.S. Geological Survey  
1116 under NSF Cooperative Agreement EAR-1724794. Bret Pecoraro performed surveying at every  
1117 station in the MAGNET GPS Network. Constructive reviews and questions from Eileen Evans,  
1118 Zachery Lifton, Isabelle Manighetti, and the Associate Editor substantially improved this  
1119 manuscript.

1120

## 1121 **References**

1122 Altamimi, Z., Rebischung, P., Métivier, L. and Collilieux, X. (2016). ITRF2014: A new release  
1123 of the International Terrestrial Reference Frame modeling nonlinear station motions, *J.*  
1124 *Geophys. Res. - Solid Earth*, 121, 6109–6131. <https://doi.org/10.1002/2016JB013098>.  
1125 Angster, S., Wesnousky, S., Figueiredo, P., Owen, L. A., and Sawyer, T. (2020). Characterizing  
1126 strain between rigid crustal blocks in the southern Cascadia forearc: Quaternary faults and  
1127 folds of the northern Sacramento Valley, California, *Geology*, v. 49, p. 387–391.  
1128 <https://doi.org/10.1130/G48114.1>.

1129 Angster, S.J, Wesnousky, S. G., Figueiredo, P. M., Owen, L. A., Hammer, S. J., (2019). Late  
1130 Quaternary slip rates for faults of the central Walker Lane (Nevada, USA): Spatiotemporal  
1131 strain release in a strike-slip fault system, *Geosphere*, 15 (5): 1460–1478.  
1132 <https://doi.org/10.1130/GES02088.1>.

1133 Argus, D., and Gordon, R.G., (1998). Current Sierra Nevada-North America motion from very  
1134 long baseline interferometry: Implications for the kinematics of the western United States,  
1135 *Geology*, v. 19, p. 1085-1088.

1136 Argus, D. F., Landerer, F. W., Wiese, D. N., Martens, H. R., Fu, Y., Famiglietti, J. S., Thomas,  
1137 B.F., Farr, T. G., Moore, A. W., Watkins, M. M. (2017). Sustained water loss in California’s  
1138 mountain ranges during severe drought from 2012 to 2015 inferred from GPS. *J. Geophys.*  
1139 *Res.- Solid Earth*, 122, 10,559–10,585. <https://doi.org/10.1002/2017JB014424>.

1140 Bacon, S. N., and Pezzopane, S. K. (2007). A 25,000-year record of earthquakes on the Owens  
1141 Valley fault near Lone Pine, California: Implications for recurrence intervals, slip rates, and  
1142 segmentation models, *Geol. Soc. Am. Bull.*, 119(7–8), 823–847.  
1143 <https://doi.org/10.1130/B25879.1>.

1144 BARD (2014), Bay Area Regional Deformation Network. UC Berkeley Seismological  
1145 Laboratory, [Dataset], <https://doi.org/10.7932/BARD>.

1146 Beanland, S., and Clark, M. M. (1994). The Owens Valley fault zone, eastern California, and  
1147 surface rupture associated with the 1872 earth- quake, *U.S. Geol. Surv. Bull.*, 1982, 29 pp.

1148 Beavan, J. and Haines, J. (2001). Contemporary horizontal velocity and strain rate fields of the  
1149 Pacific-Australian plate boundary zone through New Zealand, *J. Geophys. Res.*, 106(B1),  
1150 741– 770. <https://doi.org/10.1029/2000JB900302>.

- 1151 Bell, J.W., Caskey, S. J., Ramelli, A. R. & Guerrieri, L. (2004). Pattern and rates of faulting in  
1152 the Central Nevada Seismic Belt, and Paleoseismic Evidence for Prior Beltlike Behavior,  
1153 *Bull. Seis. Soc. Am.*, v. 94, n. 4, pp. 1229–1254.
- 1154 Bennett, R. A., Rodi, W., Reilinger, R.E. (1996). Global Positioning System constraints on fault  
1155 slip rates in southern California and northern Baja, Mexico, *J. Geophys. Res.* v. 101, B10,  
1156 21,943-21,960.
- 1157 Bennett, R. A., Wernicke, B. P., Niemi, N. A., Friedrich, A. M., and Davis, J. L. (2003).  
1158 Contemporary strain rates in the northern Basin and Range province from GPS data,  
1159 *Tectonics*, 22(2), 1008. <https://doi.org/10.1029/2001TC001355>.
- 1160 Bennett, R. A., (2007). Instantaneous slip rates from geology and geodesy, *Geophys. J. Int.*, 169,  
1161 19-28. <https://doi.org/10.1111/j.1365-246X.2007.03331.x>.
- 1162 Bertiger, W., Bar-Sever, Y., Dorsey, A., Haines, B., Harvey, N., Hemberger, D., Heflin, M., Lu,  
1163 W., Miller, M., Moore, A. W., Murphy, D., Ries, P., Romans, L., Sibois, A., Sibthorpe, A.,  
1164 Szilagy, B., Vallisneri, M., Willis, P., (2020). GipsyX/RTGx, a new tool set for space  
1165 geodetic operations and research, *Adv. Space Res.*, v. 66(3), p. 469-489, [Software],  
1166 <https://doi.org/10.1016/j.asr.2020.04.015>.
- 1167 Blewitt, G., C. Kreemer, and W.C. Hammond (2009). Geodetic observation of contemporary  
1168 deformation in the northern Walker Lane: 1. Semipermanent GPS strategy, p. 1–15,  
1169 [https://doi.org/10.1130/2009.2447\(01\)](https://doi.org/10.1130/2009.2447(01)).
- 1170 Blewitt, G., Kreemer, C., Hammond, W.C., Gazeaux, J. (2016). MIDAS Robust trend estimator  
1171 for accurate GPS station velocities without step detection, *J. Geophys. Res.- Solid Earth*, 121,  
1172 2054-2068. <https://doi.org/10.1002/2015JB012552>.

1173 Blewitt, G., Hammond, W.C. Kreemer, C. (2018). Harnessing the GPS Data Explosion for  
1174 Interdisciplinary Science, *Eos*, 99, [Dataset]. <https://doi.org/10.1029/2018EO104623>.

1175 Bormann, J., Hammond, W.C., Kreemer, C., Blewitt, G. (2016). Accommodation of missing  
1176 shear strain in the Central Walker Lane, western North America: Constraints from dense GPS  
1177 measurements, *Earth Planet. Sci. Lett.* 440, 169–177.  
1178 <https://doi.org/10.1016/j.epsl.2016.01.015>.

1179 Carlson, C. W., Pluhar, C. J., Glen, J. M. G., & Farner, M. J. (2013). Kinematics of the west-  
1180 central Walker Lane: Spatially and temporally variable rotations evident in the Late Miocene  
1181 Stanislaus Group. *Geosphere*, 9(6), 1530–1551. <https://doi.org/10.1130/GES00955.1>.

1182 Cashman, P. H., & Fontaine, S. A. (2000). Strain partitioning in the northern Walker Lane,  
1183 western Nevada and north-eastern California. *Tectonophysics*, 326, 11–130.

1184 Chanard, K., Fleitout, L., Calais, E., Reischung, P., & Avouac, J.-P. (2018). Toward a global  
1185 horizontal and vertical elastic load deformation model derived from GRACE and GNSS  
1186 station position time series. *J. Geophys. Res. - Solid Earth*, 123, 3225–3237.  
1187 <https://doi.org/10.1002/2017JB015245>.

1188 DeLano, K., Lee, J., Roper, R., and Calvert, A., (2019). Dextral, normal, and sinistral faulting  
1189 across the eastern California shear zone–Mina deflection transition, California-Nevada, USA:  
1190 *Geosphere*, v. 15(4), p. 1–34. <https://doi.org/10.1130/GES01636.1>.

1191 deMets, C. and Merkouriev, S., (2016). High-resolution reconstructions of Pacific–North  
1192 America plate motion: 20 Ma to present, *Geophys. J. Int.*, 207, 741–773.  
1193 <https://doi.org/10.1093/gji/ggw305>.

1194 dePolo, C. M. (2008). Quaternary Faults in Nevada, Nevada Bureau of Mines and Geology,  
1195 University of Nevada, Reno, map 167, scale 1:1,000,000.  
1196 <https://pubs.nbmng.unr.edu/Quaternary-faults-in-Nevada-p/m167.htm>.

1197 dePolo, D.M, and dePolo, C. M., (2012). Earthquakes in Nevada, 1840s to 2010, Nevada  
1198 Seismological Laboratory and the Nevada Bureau of Mines and Geology, University of  
1199 Nevada, Reno, map 179, scale 1:1,000,000. [https://pubs.nbmng.unr.edu/Earthquakes-in-NV-](https://pubs.nbmng.unr.edu/Earthquakes-in-NV-1840s-to-2010-p/m179.htm)  
1200 [1840s-to-2010-p/m179.htm](https://pubs.nbmng.unr.edu/Earthquakes-in-NV-1840s-to-2010-p/m179.htm).

1201 Dixon, T.H., Miller, M., Farina, F., Wang, H., Johnson, D., (2000). Present-day motion of the  
1202 Sierra Nevada block and some tectonic implications for the Basin and Range province, North  
1203 American Cordillera, *Tectonics*, v. 19. n.1, 1-24, 1998TC001088.

1204 Dill, R., and Dobslaw, H. (2013). Numerical simulations of global-scale high-resolution  
1205 hydrological crustal deformations, [Dataset], *J. Geophys. Res. - Solid Earth*, 118, 5008–5017.  
1206 <https://doi.org/10.1002/jgrb.50353>.

1207 Dokka, R. K., Travis, C. J. (1990). Role of the Eastern California Shear Zone in accommodating  
1208 Pacific-North America plate motion, *Geophys. Res. Lett.*, 17(9), p.1323-1326, 90GL01331.

1209 Evans, E., Loveless, J.P., Meade, B.J. (2015). Total variation regularization of geodetically and  
1210 geologically constrained block models for the Western United States, *Geophys. J. Int.*, 202,  
1211 713–727.

1212 Evans, E.L. (2022). A dense block model representing western continental United States  
1213 deformation for the 2023 update to the National Seismic Hazard Model, *Seismol. Res. Lett.*,  
1214 93(6), 3024–3036. <https://doi.org/10.1785/0220220141>.

1215 Faulds, J. E., & Henry, C. D. (2008). Tectonic influences on the spatial and temporal evolution  
1216 of the Walker Lane: An incipient transform fault along the evolving Pacific–North American

1217 plate boundary, in Spencer, J.E., and Titley, S.R., eds. Ores and orogenesis: Circum-Pacific  
1218 tectonics, geologic evolution, and ore deposits: *Arizona Geological Society Digest*, 22, 437–  
1219 470.

1220 Field, E. H., Milner, K. R., Hatem, A. E., Powers, P. M., Pollitz, F. F., Llenos, A. L., Zeng, Y.,  
1221 Johnson, K. M., Shaw, B. E., McPhillips, D., Thompson Jobe, J., Shumway, A. M., Michael,  
1222 A. J., Shen, Z.-K., Evans, E. L., Hearn, E. H., Mueller, C. S., Frankel, A. D., Petersen, M. D.,  
1223 DuRoss, C., Briggs, R. W., Page, M. T., Rubinstein, J. L., Herrick, J.A., (2023). The USGS  
1224 2023 Conterminous U.S. Time-Independent Earthquake Rupture Forecast, *Bull. Seismol. Soc.*  
1225 *Am.*, <https://doi.org/10.1785/0120230120>.

1226 Foy, T. A., Frankel, K. L., Lifton, Z. M., Johnson, C. W., and Caffee, M. W. (2012). Distributed  
1227 extensional deformation in a zone of right-lateral shear: Implications for geodetic versus  
1228 geologic rates of deformation in the eastern California shear zone-Walker Lane, *Tectonics*,  
1229 *31*, TC4008. <https://doi.org/10.1029/2011TC002930>.

1230 Frankel A. D., Petersen, M. D., Mueller, C. S., Haller, K. M., Wheeler, R. L., Leyendecker, E.V.,  
1231 Wesson, R. L., Harmsen, S. C., Cramer, C. H., Perkins, D. M., and Rukstales, K. S. (2002).  
1232 Documentation for the 2002 update of the National Seismic Hazard Maps, Open-File Report  
1233 02-420.

1234 Gourmelen, N., and Amelung, F. (2005). Postseismic mantle relaxation in the Central Nevada  
1235 Seismic Belt, *Science*, *310*, 1473-1476.

1236 Haddon, E. K., Amos, C. B., Zielke, O., Jayko, A.S. and Bürgmann, R. (2016). Surface slip  
1237 during large Owens Valley earthquakes, *Geochem. Geophys. Geosyst.*, *17*, 2239–2269.  
1238 <https://doi.org/10.1002/2015GC006033>.

1239 Hammond, W. C., and Thatcher, W. (2005). Northwest Basin and Range tectonic deformation  
1240 observed with the Global Positioning System, 1999–2003, *J. Geophys. Res. - Solid Earth*,  
1241 *110*, B10405. <https://doi.org/10.1029/2005JB003678>.

1242 Hammond, W. C., and Thatcher, W. (2007). Crustal deformation across the Sierra Nevada,  
1243 northern Walker Lane, Basin and Range transition, western United States measured with  
1244 GPS, 2000–2004, *J. Geophys. Res. - Solid Earth*, *112*, B05411.  
1245 <https://doi.org/10.1029/2006JB004625>.

1246 Hammond, W.C., Kreemer, C., and Blewitt, G. (2009). Geodetic constraints on contemporary  
1247 deformation in the northern Walker Lane: 3. Central Nevada Seismic Belt postseismic  
1248 relaxation, *in* Oldow, J.S., and Cashman, P.H., eds., *Late Cenozoic Structure and Evolution*  
1249 *of the Great Basin – Sierra Nevada Transition*, Geological Society of America, Special Paper  
1250 447, p. 33–54. [https://doi.org/10.1130/2009.2447\(03\)](https://doi.org/10.1130/2009.2447(03)).

1251 Hammond, W. C., Blewitt, G., Kreemer, C. (2011). Block modeling of crustal deformation of the  
1252 northern Walker Lane and Basin and Range from GPS velocities, *J. Geophys. Res.*, *116*,  
1253 B04402. <https://doi.org/10.1029/2010JB007817>.

1254 Hammond, W.C., Blewitt, G., Kreemer, C. (2014). Steady contemporary deformation of the  
1255 central Basin and Range Province, western United States, *J. Geophys. Res.*, *119*, 5235-5253,  
1256 <https://doi.org/10.1002/2014JB011145>.

1257 Hammond, W.C., Blewitt, G., Kreemer, C. (2016). GPS Imaging of vertical land motion in  
1258 California and Nevada: Implications for Sierra Nevada uplift, *J. Geophys. Res.*, - *Solid Earth*,  
1259 *121*, n. 10, p. 7681-7703. <https://doi.org/10.1002/2016JB013458>.

1260 Hammond, W.C., Kreemer, C., Zaliapin, I., Blewitt, G. (2019). Drought-triggered magmatic  
1261 inflation, crustal strain and seismicity near the Long Valley Caldera, Central Walker Lane, *J.*  
1262 *Geophys. Res. - Solid Earth*, 124(6), p. 6072–6091. <https://doi.org/10.1029/2019JB017354>.

1263 Hammond, W., Blewitt, G., & Kreemer, C. (2024). GPS Imaging software [Software]. *Zenodo*.  
1264 <https://doi.org/10.5281/zenodo.10672265>.

1265 Hammond, W., Blewitt, G., & Kreemer, C. (2024). Block modeling software (v1.0) [Software].  
1266 *Zenodo*. <https://doi.org/10.5281/zenodo.10672393>.

1267 Hatem, A. E., & Dolan, J. F. (2018). A model for the initiation, evolution, and controls on  
1268 seismic behavior of the Garlock fault, California. *Geochem., Geophys., Geosys.*, 19, 2166–  
1269 2178. <https://doi.org/10.1029/2017GC007349>.

1270 Hatem, A.E., Collett, C.M., Briggs, R.W., Gold, R.D., Angster, S.J., Powers, P.M., Field, E.H.,  
1271 Anderson, M., Ben-Horin, J.Y., Dawson, T., DeLong, S., DuRoss, C., Thompson Jobe, J.,  
1272 Kleber, E., Knudsen, K.L., Koehler, R., Koning, D., Lifton, Z., Madin, I., Mauch, J., Morgan,  
1273 M., Pearthree, P., Pollitz, F., Scharer, K., Sherrod, B., Stickney, M., Wittke, S., and  
1274 Zachariasen, J., (2022a). Earthquake geology inputs for the U.S. National Seismic Hazard  
1275 Model (NSHM) 2023 (western US) (ver. 2.0, February 2022): U.S. Geological Survey data  
1276 release, [Dataset]. <https://doi.org/10.5066/P9AU713N>.

1277 Hatem, A.E., Reitman, N.G., Briggs, R.W., Gold, R.D., Thompson Jobe, J.A., and Burgette, R.J.,  
1278 (2022b). Western U.S. geologic deformation model for use in the U.S. National Seismic  
1279 Hazard Model 2023, version 1.0: U.S. Geological Survey Data Release.  
1280 <https://doi.org/10.5066/P9W63WOZ>.

1281 Hatem, A. E., Collett, C. M., Briggs, R. W., Gold, R. D., Field, E. H., Powers, P. M., and the  
1282 Earthquake Geology Working Group (2022c). Simplifying complex fault data for systems-

1283 level analysis: Earthquake geology inputs for U.S. NSHM 2023, *Sci. Data* 9, 506.  
1284 <https://doi.org/10.1038/s41597-022-01609-7>.

1285 Hearn, E., K. Johnson, D. Sandwell, and W. Thatcher (2010). SCEC UCERF Workshop Report,  
1286 [http://www.scec.org/workshops/2010/gps-ucerf3/FinalReport\\_GPS-UCERF3Workshop.pdf](http://www.scec.org/workshops/2010/gps-ucerf3/FinalReport_GPS-UCERF3Workshop.pdf)

1287 Hearn, E., (2022). “Ghost Transient” Corrections to the Southern California GPS velocity field  
1288 from San Andreas Fault seismic cycle models, *Seis. Res. Lett.*, 93 (6): 2973–2989.  
1289 <https://doi.org/10.1785/0220220156>.

1290 Hudnut, K. W., N. E. King, J. E. Galetzka, K. F. Stark, J. A. Behr, A. Aspiotes, S. van Wyk, R.  
1291 Moffitt, S. Dockter, and F. Wyatt, (2002). Continuous GPS observations of postseismic  
1292 deformation following the 16 October 1999 Hector Mine, California, earthquake (Mw7.1),  
1293 *Bull. Seismol. Soc. Amer.*, v. 92(4), 1403-1422, <https://doi.org/10.1785/0120000912>.

1294 Husson, L., Bodin, T., Spada, G., Choblet, G., Kreemer, C. (2018). Bayesian surface  
1295 reconstruction of geodetic uplift rates: Mapping the global fingerprint of Glacial Isostatic  
1296 Adjustment, *J. Geodynamics*, 122, 25-40. <https://doi.org/10.1016/j.jog.2018.10.002>.

1297 Jayko, A.S., (2009). Deformation of the late Miocene to Pliocene Inyo Surface, eastern Sierra  
1298 region, California, in Oldow, J.S., and Cashman, P., eds., Late Cenozoic structure and  
1299 evolution of the Great Basin–Sierra Nevada transition: Geological Society of America  
1300 Special Paper 447, p. 313–350.

1301 Johnson, K. M., Hammond, W. C. and Weldon, R. J. (2024). Review of geodetic and geologic  
1302 deformation models for 2023 US National Seismic Hazard Model, *Bull. Seis. Soc.*  
1303 *Am.*, <https://doi.org/10.1785/0120230137>.

1304 Koehler, R.D., and Wesnousky, S. (2011). Late Pleistocene regional extension rate derived from  
1305 earthquake geology of late Quaternary faults across the Great Basin, Nevada, between

1306 38.5°N and 40°N latitude, *GSA Bulletin*, v. 123, no. 3/4, p. 631–650.  
1307 <https://doi.org/10.1130/B30111.1>.

1308 Koehler, R. D., Dee, S., Elliott, A., Hatem, A., Pickering, A., Pierce, I., and Seitz, G. (2021).  
1309 Field response and surface-rupture characteristics of the 2020 M 6.5 Monte Cristo Range  
1310 Earthquake, Central Walker Lane, Nevada, *Seismol. Res. Lett.* 92(2A), 823–839.  
1311 <https://doi.org/10.1785/0220200371>.

1312 Kreemer, C., Blewitt, G., Hammond, W. C. (2010). Evidence for an active shear zone in  
1313 southern Nevada linking the Wasatch fault to the Eastern California shear zone. *Geology*,  
1314 38(5), 475–478. <https://doi.org/10.1130/G30477.1>.

1315 Kreemer, C., Hammond, W.C., Blewitt, G., Holland, A. Bennett, R.A., (2012). A geodetic strain  
1316 rate model for the southwestern United States, scale 1:1,500,000, Nevada Bureau of Mines  
1317 and Geology publication M178.

1318 Kreemer, C., Blewitt, G. and Klein, E. C. (2014). A geodetic plate motion and Global Strain Rate  
1319 Model, *Geochem. Geophys. Geosyst.*, 15, 3849–3889.  
1320 <https://doi.org/10.1002/2014GC005407>.

1321 Kreemer, C., Hammond, W. C., & Blewitt, G. (2018). A robust estimation of the 3-D intraplate  
1322 deformation of the North American plate from GPS. *J. Geophys. Res.-Solid Earth*, 123,  
1323 <https://doi.org/10.1029/2017JB015257>.

1324 Kreemer, C., Blewitt, G., Davis, P. M. (2020). Geodetic evidence for a buoyant mantle plume  
1325 beneath the Eifel volcanic area, NW Europe, *Geophys. J. Int.*, 222, 1316–1332.  
1326 <https://doi.org/10.1093/gji/ggaa227>.

1327 Kreemer, C., and Z. M. Young (2022). Crustal strain rates in the Western United States and their  
1328 relationship with earthquake rates, *Seis. Res. Lett.*, 1–19.  
1329 <https://doi.org/10.1785/0220220153>.

1330 Lee, J., Pencer, J., & Owens, L. (2001). Holocene slip rates along the Owens Valley fault,  
1331 California: Implications for the recent evolution of the eastern California shear zone.  
1332 *Geology*, 29, 819–822.

1333 Lifton, Z. M., Newman, A. V., Frankel, K. L., Johnson, C. W., and Dixon, T. H. (2013). Insights  
1334 into distributed plate rates across the Walker Lane from GPS geodesy, *Geophys. Res. Lett.*,  
1335 40, 4620–4624. <https://doi.org/10.1002/grl.50804>.

1336 Lifton, Z.M., Frankel, K.L., and Newman, A.V. (2015). Latest Pleistocene and Holocene slip  
1337 rates on the Lone Mountain fault: Evidence for accelerating slip in the Silver Peak-Lone  
1338 Mountain extensional complex: *Tectonics*, v. 34, no. 3, p. 449–463.  
1339 <https://doi.org/10.1002/2013TC003512>.

1340 Lisowski, M., 2012, CVO GPS Network - The GAGE Facility operated by EarthScope  
1341 Consortium, GPS/GNSS Observations, [Dataset]. <https://doi.org/10.7283/T5BP00ZC>.

1342 Loveless, J. P., and Meade, B. J. (2010). Geodetic imaging of plate motions, slip rates, and  
1343 partitioning of deformation in Japan, *J. Geophys. Res.*, 115, B02410.  
1344 <https://doi.org/10.1029/2008JB006248>.

1345 Martens, H.R., Argus, D.F., Norberg, C., Blewitt, G., Herring, T.A., Moore, A.W., Hammond,  
1346 W.C., Kreemer, C. (2020). Atmospheric pressure loading in GPS positions: dependency on  
1347 GPS processing methods and effect on assessment of seasonal deformation in the contiguous  
1348 USA and Alaska, *J. Geodesy*, 94:115. <https://doi.org/10.1007/s00190-020-01445-w>.

1349 Matsu'ura, M., Jackson, D.D., Cheng, A. (1986). Dislocation model for aseismic crustal  
1350 deformation at Hollister, California, *J. Geophys. Res.* v. 91, B12, p. 12,661-12,674.

1351 Maurer, J., and Materna, K., (2023). Quantification of geodetic strain rate uncertainties and  
1352 implications for seismic hazard estimates, *Geophys. J. Int.*, v. 234, I. 3, P. 2128–  
1353 2142. <https://doi.org/10.1093/gji/ggad191>.

1354 McCaffrey, R., (2002). Crustal block rotations and plate coupling, in *Plate Boundary Zones*, v.  
1355 30, p. 101–122, eds S. Stein & J. Freymueller, AGU Geodynamics Series

1356 McCaffrey, R., Qamar, A. I., King, R.W., Wells, R., Khazaradze, G., Williams, C. A., Stevens,  
1357 C. W., Vollick, J.J., Zwick, P.C. (2007). Fault locking, block rotation and crustal deformation  
1358 in the Pacific Northwest, *Geophys. J. Int.*, 169, 1315–1340. [https://doi.org/10.1111/j.1365-  
1359 246X.2007.03371.x](https://doi.org/10.1111/j.1365-246X.2007.03371.x).

1360 McCaffrey, R., King, R. W., Payne, S. J., and Lancaster, M. (2013). Active tectonics of  
1361 northwestern U.S. inferred from GPS-derived surface velocities, *J. Geophys. Res. - Solid  
1362 Earth*, 118. <https://doi.org/10.1029/2012JB009473>.

1363 McCaffrey, R., King, R. W., Wells, R. E., Lancaster, M., Miller, M.M. (2016). Contemporary  
1364 deformation in the Yakima fold and thrust belt estimated with GPS, *Geophys. J. Int.*, 207, 1–  
1365 11. <https://doi.org/10.1093/gji/ggw252>.

1366 McGill, S.F., Wells, S.G., Fortner, S.K., Kuzma, H. A., McGill, J. D. (2009). Slip rate of the  
1367 western Garlock fault, at Clark Wash, near Lone Tree Canyon, Mojave Desert, California,  
1368 *GSA Bulletin*, 121, 536-554. <https://doi.org/10.1130/B26123.1>.

1369 McGill, S. F., Spinler, J. C., McGill, J. D., Bennett, R. A., Floyd, M. A., Fryxell, J. E., and  
1370 Funning, G. J., (2015), Kinematic modeling of fault slip rates using new geodetic velocities  
1371 from a transect across the Pacific-North America plate boundary through the San Bernardino

1372 Mountains, California, *J. Geophys. Res. Solid Earth*, *120*, 2772–2793.  
1373 <https://doi.org/10.1002/2014JB011459>.

1374 McKenzie, D., and Jackson, J. (1983). The relationship between strain rates, crustal thickening,  
1375 paleomagnetism, finite strain and fault movements within a deforming zone, *Earth Planet.*  
1376 *Sci. Lett.*, *65*, 182-202.

1377 Meade, B. J., and Hager, B. H. (2005). Block models of crustal motion in southern California  
1378 constrained by GPS measurements, *J. Geophys. Res.* *110*, B03403.  
1379 <http://doi.org/10.1029/2004JB003209>.

1380 Montgomery-Brown, E. K., Wicks, C. W., Cervelli, P. F., Langbein, J. O., Svarc, J. L., Shelly,  
1381 D. R., Hill, D. P., and Lisowski, M. (2015). Renewed inflation of Long Valley Caldera,  
1382 California (2011 to 2014), *Geophys. Res. Lett.*, *42*, 5250–5257.  
1383 <https://doi.org/10.1002/2015GL064338>.

1384 Murray, J. R., and Svarc, J. (2017). Global Positioning System data collection, processing, and  
1385 analysis conducted by the U.S. Geological Survey Earthquake Hazards Program, *Seis. Res.*  
1386 *Lett.*, *88* (3): 916–925. <https://doi.org/10.1785/0220160204>.

1387 Neely, W. R., Borsa, A. A., Burney, J. A., Levy, M. C., Silverii, F., & Sneed, M. (2021).  
1388 Characterization of groundwater recharge and flow in California's San Joaquin Valley from  
1389 InSAR-observed surface deformation. *Water Resources Res.*, *57*, e2020WR028451. <https://doi.org/10.1029/2020WR028451>.  
1390 [doi.org/10.1029/2020WR028451](https://doi.org/10.1029/2020WR028451).

1391 NOAA National Geodetic Survey (NGS), (1994). NOAA Archive of NGS National  
1392 Continuously Operating Reference Station (CORS) Network (NCN) [Dataset], *NOAA*  
1393 *National Centers for Environmental Information*. <https://doi.org/10.25921/wc4r-ee36>.

1394 Okada, Y. (1985), Surface deformation due to shear and tensile faults in a half-space, *Bull. Seis.*  
1395 *Soc. Am.*, 75, 1135-1154.

1396 Oldow, J.S., (1992). Late Cenozoic displacement partitioning in the northwestern Great Basin, in  
1397 Lane, C., and Steven, D., eds., Geological Society of Nevada Walker Lane Symposium:  
1398 Structure, Tectonics and Mineralization of the Walker Lane: Reno, Nevada, Geological  
1399 Society of Nevada, p. 17–52.

1400 Oldow, J.S., Kohler, G., Donelick, R.A., (1994). Late Cenozoic extensional transfer in the  
1401 Walker Lane strike-slip belt, Nevada, *Geology*, v. 22, p. 637-640.

1402 Oldow, J. S. (2003). Active transtensional boundary zone between the western Great Basin and  
1403 Sierra Nevada block, western US Cordillera. *Geology*, 31(12), 1033–1036.  
1404 <https://doi.org/10.1130/G19838.1>.

1405 Oskin, M., Perg, L., Blumentritt, D., Mukhopadhyay, S., and Iriondo, A. (2007). Slip rate of the  
1406 Calico fault: Implications for geologic versus geodetic rate discrepancy in the Eastern  
1407 California Shear Zone, *J. Geophys. Res.*, 112, B03402.  
1408 <https://doi.org/10.1029/2006JB004451>.

1409 Pancha, A., Anderson, J.G., Kreemer, C., (2006). Comparison of seismic and geodetic scalar  
1410 moment rates across the Basin and Range Province, *Bull. Seis. Soc. Am.*, v. 96, n.1, p. 11-32.  
1411 <https://doi.org/10.1785/0120040166>.

1412 PANGA- Pacific Northwest Geodetic Array (1996). GPS/GNSS Network and Geodesy  
1413 Laboratory: Central Washington University, other/seismic network, [Dataset], *Int. Fed. of*  
1414 *Digital Seismograph Networks*, <https://doi.org/10.7914/SN/PW>.

1415 Personius, S. F., Crone, A. J., Machette, M. N., Mahan, S. A., Kyung, J.B., Cisneros, H., and  
1416 Lidke, D. J., (2007). Late Quaternary Paleoseismology of the Southern Steens Fault Zone,

1417 Northern Nevada, *Bull. Seis. Soc. Am.*, v. 97, n. 5, pp. 1662–1678.  
1418 <https://doi.org/10.1785/0120060202>.

1419 Personius, S. F., Crone, A. J., Machette, M. N., Mahan, S. A. and Lidke, D. J. (2009). Moderate  
1420 rates of late Quaternary slip along the northwestern margin of the Basin and Range Province,  
1421 Surprise Valley fault, northeastern California, *J. Geophys. Res.*, 114, B09405.  
1422 <https://doi.org/10.1029/2008JB006164>.

1423 Petersen, M.D., Moschetti, M.P., Powers, P.M., Mueller, C.S., Haller, K.M., Frankel, A.D.,  
1424 Zeng, Yuehua, Rezaeian, Sanaz, Harmsen, S.C., Boyd, O.S., Field, Ned, Chen, Rui,  
1425 Rukstales, K.S., Luco, Nico, Wheeler, R.L., Williams, R.A., and Olsen, A.H., (2014).  
1426 Documentation for the 2014 update of the United States national seismic hazard maps: U.S.  
1427 Geological Survey Open-File Report 2014–1091, 243 p.  
1428 <https://doi.org/10.3133/ofr20141091>.

1429 Petronis, M. S., Geissman, J. W., Oldow, J. S., & McIntosh, W. C. (2009). Late Miocene to  
1430 Pliocene vertical-axis rotation attending development of the Silver Peak–Line Mountain  
1431 displacement transfer zone, west-central Nevada. In J. S. Oldow, & P. H. Cashman (Eds.),  
1432 Late Cenozoic Structure and Evolution of the Great Basin–Sierra Nevada Transition (pp.  
1433 215–254). Colorado, USA, Special Paper 447: Geological Society of America.  
1434 [https://doi.org/10.1130/2009.2447\(12\)](https://doi.org/10.1130/2009.2447(12)).

1435 Pierce, I. K. D., Wesnousky, S. G., Owen, L. A., Bormann, J. M., Li, X., & Caffee, M. (2021).  
1436 Accommodation of plate motion in an incipient strike- slip system: The Central Walker Lane.  
1437 *Tectonics*, 40, e2019TC005612. <https://doi.org/10.1029/2019TC005612>.

1438 Platt, J.P., and Becker, T. (2013). Kinematics of rotating panels of E–W faults in the San  
1439 Andreas system: What can we tell from geodesy? *Geophys. J. Int.*, 194, 1295–1301.  
1440 <https://doi.org/10.1093/gji/ggt189>.

1441 Pollitz, F.F., (1997). Gravitational-viscoelastic postseismic relaxation on a layered spherical  
1442 Earth: *J. Geophys. Res.*, v. 102, p. 17,921– 17,941, [Software].  
1443 <https://doi.org/10.1029/97JB01277>.

1444 Pollitz, F.F., (2022a). Viscoelastic fault-based model of crustal deformation for the 2023 update  
1445 to the US National Seismic Hazard Model, *Seis. Res. Lett.* 93 (6), 3087–3099.  
1446 <https://doi.org/10.1785/0220220137>.

1447 Pollitz, F.F., Evans, E.L., Field, E.H., Hatem, A.E., Hearn, E.H., Johnson, K., Murray, J.R.,  
1448 Powers, P.N., Shen, Z.-K., Wespestad, C., Zeng, Y. (2022b). Western US deformation  
1449 models for the 2023 update to the US National Seismic Hazard Model, *Seis. Res. Lett.* 93 (6),  
1450 3068–3086. <https://doi.org/10.1785/0220220143>.

1451 Ruhl, C. J., Abercrombie, R., Hatch, R., & Smith, K. (2020). Relocated Earthquake Catalog -  
1452 Seismogenic Depth Variation across the Transtensional Northern Walker Lane (1.0) [Data  
1453 set]. *Zenodo*. <https://doi.org/10.5281/zenodo.4141086>.

1454 Sandwell, D. T., Zeng, Y., Shen, Z.-K., Crowell, B., Murray, J., McCaffrey, R., & Xu, X. (2016).  
1455 "The SCEC Community Geodetic Model V1: Horizontal Velocity Grid".  
1456 [https://topex.ucsd.edu/CGM/technical\\_report/CGM\\_V1.pdf](https://topex.ucsd.edu/CGM/technical_report/CGM_V1.pdf).

1457 Savage, J.C. and Burford, R.O. (1973). Geodetic determination of relative plate motion in  
1458 Central California, *J. Geophys. Res.*, v. 78, n. 5. p. 832-845.

1459 Savage, J.C., (1983). A dislocation model of strain accumulation and release at a Subduction  
1460 zone, *J. Geophys. Res.*, v. 88, n. B6. p. 4984-4996.

1461 Savage, J.C., Gan, W. and Svarc, J. L. (2001). Strain accumulation and rotation in the eastern  
1462 California shear zone, *J. Geophys. Res.*, *106*, 21,995–22,007.

1463 Seitz, G., Kent, G., Driscoll, N., Dingler, J. (2016). Large earthquakes on the Incline Village  
1464 Fault from onshore and offshore paleoseismology, Lake Tahoe, California-Nevada, Chapter  
1465 43, Applied Geology in California, AEG Special Publication Number 26, R. Anderson, H.  
1466 Ferriz eds.

1467 Shen, Z.-K., Jackson, D.D., Ge, B.X. (1996). Crustal deformation across and beyond the Los  
1468 Angeles basin from geodetic measurements, *J. Geophys. Res.*, *v101*, n. B12, p 27,957-  
1469 27,980.

1470 Shen, Z.-K., Jackson, D.D., Kagan, Y.Y. (2007). Implications of Geodetic strain rate for future  
1471 earthquakes, with a five-year forecast of M5 earthquakes in southern California, *Seis. Res.*  
1472 *Lett.*, *78*(1). <https://doi.org/10.1785/gssrl.78.1.116>.

1473 Shen, Z.-K., King, R. W., Agnew, D. C., Wang, M., Herring, T. A., Dong, D. and Fang, P.  
1474 (2011), A unified analysis of crustal motion in Southern California, 1970–2004: The SCEC  
1475 crustal motion map, *J. Geophys. Res. - Solid Earth*, *116*, B11402.  
1476 <https://doi.org/10.1029/2011JB008549>.

1477 Shen, Z.-K., Wang, M., Zeng, Y., Wang, F. (2015). Optimal interpolation of spatially discretized  
1478 Geodetic data, *Bull. Seis. Soc. Am.*, *105* (4): 2117–2127. <https://doi.org/10.1785/0120140247>.

1479 Shen, Z.-K., and Bird, P. (2022). NeoKinema deformation model for the 2023 update to the US  
1480 National Seismic Hazard Model, *Seismol. Res. Lett.*, *93*(6), 3037–3052.  
1481 <https://doi.org/10.1785/0220220179>.

1482 Spinler, J. C., Bennett, R. A., Anderson, M. L., McGill, S. F., Hreinsdóttir, S. and McCallister,  
1483 A. (2010). Present-day strain accumulation and slip rates associated with southern San

1484 Andreas and eastern California shear zone faults, *J. Geophys. Res.- Solid Earth*, 115,  
1485 B11407. <https://doi.org/10.1029/2010JB007424>.

1486 Slemmons, D.B., Jones, A.E., and Gimlett, J.I. (1965). Catalog of Nevada earthquakes, 1852–  
1487 1960: *Geol. Soc. Am. Bull.*, v. 55, p. 537–583.

1488 Spakman, W. & Nyst, M.C.J., (2002). Inversion of relative motion data for estimates of the  
1489 velocity gradient field and fault slip, *Earth planet. Sci. Lett.*, 203, 577–591.  
1490 [https://doi.org/10.1016/S0012-821X\(02\)00844-0](https://doi.org/10.1016/S0012-821X(02)00844-0).

1491 Stewart, J.H., (1988). Tectonics of the Walker Lane belt, western Great Basin: Mesozoic and  
1492 Cenozoic deformation in a zone of shear, in Ernst, W. G., ed., *Metamorphism and crustal*  
1493 *evolution of the west- ern United States*: Prentice Hall, Englewood Cliffs, New Jersey, p.  
1494 681-713.

1495 Surpress, B., (2008). Modern strain localization in the central Walker Lane, western United  
1496 States: Implications for the evolution of intraplate deformation in transtensional settings,  
1497 *Tectonophysics* 457, 239–253. <https://doi.org/10.1016/j.tecto.2008.07.001>.

1498 Tape, C., Musé, P., Simons, M., Dong, D., Webb, R., (2009). Multiscale estimation of GPS  
1499 velocity fields, *Geophys. J. Int.*, 179(2), 945–971. [https://doi.org/10.1111/j.1365-](https://doi.org/10.1111/j.1365-246X.2009.04337.x)  
1500 [246X.2009.04337.x](https://doi.org/10.1111/j.1365-246X.2009.04337.x).

1501 Thatcher, W., Foulger, G., Julian, B., Svarc, J., Quility, E., Bawden, G. (1999). Present-day  
1502 deformation across the Basin and Range Province, western U.S. *Science*, 283(5408), 1714–  
1503 1718. <https://doi.org/10.1126/science.283.5408.1714>.

1504 UNAVCO Community, (2007). PBO GPS Network - The GAGE Facility operated by  
1505 EarthScope Consortium, GPS/GNSS Observations, [Dataset].  
1506 <https://doi.org/10.7283/T5X63K0F>.

1507 Unruh, J., Humphrey, J., Barron, A. (2003). Transtensional model for the Sierra Nevada frontal  
1508 fault system, eastern California, *Geology*, v. 31, n. 4, p. 327–330.

1509 Unruh, J., Hauksson, E., Jones, C.H. (2014). Internal deformation of the southern Sierra Nevada  
1510 microplate associated with foundering lower lithosphere, California *Geosphere*, v. 10, no. 1,  
1511 p. 107–128. <https://doi.org/10.1130/GES00936.1>.

1512 Unruh, J. and Humphrey, J. (2017). Seismogenic deformation between the Sierran microplate  
1513 and Oregon Coast block, California, USA, *Geology*, v. 45, n. 5, p. 415–418.  
1514 <https://doi.org/10.1130/G38696.1>.

1515 U.S. Geological Survey and Nevada Bureau of Mines and Geology, Quaternary Fault and Fold  
1516 Database for the United States, accessed April, 2011, [Dataset].  
1517 <https://www.usgs.gov/natural-hazards/earthquake-hazards/faults>.

1518 U.S. Geological Survey and California Geological Survey, Quaternary Fault and Fold Database  
1519 for the United States, accessed April, 2011, [Dataset]. [https://www.usgs.gov/natural-](https://www.usgs.gov/natural-hazards/earthquake-hazards/faults)  
1520 [hazards/earthquake-hazards/faults](https://www.usgs.gov/natural-hazards/earthquake-hazards/faults).

1521 U.S. Geological Survey and Utah Geological Survey, Quaternary Fault and Fold Database for the  
1522 United States, accessed April, 2011, [Dataset]. At: [https://www.usgs.gov/natural-](https://www.usgs.gov/natural-hazards/earthquake-hazards/faults)  
1523 [hazards/earthquake-hazards/faults](https://www.usgs.gov/natural-hazards/earthquake-hazards/faults).

1524 U.S. Geological Survey and Arizona Geological Survey, Quaternary Fault and Fold Database for  
1525 the United States, accessed April, 2011, [Dataset]. [https://www.usgs.gov/natural-](https://www.usgs.gov/natural-hazards/earthquake-hazards/faults)  
1526 [hazards/earthquake-hazards/faults](https://www.usgs.gov/natural-hazards/earthquake-hazards/faults).

1527 Wallace, R.E., (1984). Patterns and timing of Late Quaternary faulting in the Great Basin  
1528 Province and relation to some regional tectonic features, *J. Geophys. Res.*, v. 89, n. B7, p.  
1529 5763-5769.

- 1530 Ward, S.N. (1998). On the consistency of earthquake moment rates, geological fault data, and  
1531 space geodetic strain: the United States. *Geophys. J. Int.* 134, 172-186.
- 1532 Weldon, R.J., Humphreys, E.D., (1986). A kinematic model of Southern California, *Tectonics*,  
1533 5(1), p. 33-48, 5T0745.
- 1534 Wernicke, B., Friedrich, A.M., Niemi, N.A., Bennett, R.A., Davis, J.L., (2000). Dynamics of  
1535 plate boundary fault systems from Basin and Range Geodetic network (BARGEN and  
1536 geologic data, *GSA Today*, v. 10(11).
- 1537 Wesnousky, S. G. (2005). Active faulting in the Walker Lane. *Tectonics*, 24, TC3009.  
1538 <https://doi.org/10.1029/2004TC001645>.
- 1539 Wesnousky, S. G., Bormann, J. M., Kreemer, C., Hammond, W. C. and Brune, J. N. (2012).  
1540 Neotectonics, geodesy, seismic hazard in the northern Walker Lane of western North  
1541 America: Thirty kilometers of crustal shear and no strike-slip? *Earth and Planetary Science  
1542 Letters*, 329-330. <https://doi.org/10.1016/j.epsl.2012.02.018>.
- 1543 Wessel, P., Smith, W. H. F., Scharroo, R., Luis, J. and Wobbe, F. (2013). Generic Mapping  
1544 Tools: Improved Version Released, *EOS Trans. AGU*, 94(45), p. 409-410, [Software].  
1545 <https://doi.org/10.1002/2013EO450001>.
- 1546 Wicks, C. W., Thatcher, W., Monastero, F.C., Hasting, M.A. (2001). Steady state deformation of  
1547 the Coso Range, east central California, inferred from satellite radar interferometry, *J.  
1548 Geophys. Res.*, v. 106, n. B7, p. 13,769-13,780.
- 1549 Wilcox, R. R. (2005). Introduction to robust estimation and hypothesis testing, Elsevier  
1550 Academic Press, Burlington, Mass.
- 1551 Williams, T. B., Kelsey, H. M., and Freymueller, J. T. (2006). GPS-derived strain in  
1552 northwestern California and convergence of the Sierra Nevada–Great Valley block contribute

1553 to southern Cascadia forearc contraction: *Tectonophysics*, v. 413, p. 171–184.  
1554 <https://doi.org/10.1016/j.tecto.2005.10.047>.

1555 Young, Z., Kreemer, C., Hammond, W. C. and Blewitt, G. (2023). Interseismic strain  
1556 accumulation between the Colorado Plateau and the Eastern California Shear Zone:  
1557 Implications for the seismic hazard near Las Vegas, Nevada, *Bull. Seis. Soc. Am.*, 113(2),  
1558 856-876. <https://doi.org/10.1785/0120220136>.

1559 Zeng, Y. (2022a). A fault-based crustal deformation model with deep driven dislocation sources  
1560 for the 2023 Update to the US National Seismic Hazard Model, *Seismo. Res. Lett.*, 93 (6),  
1561 3170–3185. <https://doi.org/10.1785/0220220209>.

1562 Zeng, Y. (2022b). GPS velocity field of the western United States for the 2023 National Seismic  
1563 Hazard Model update, *Seismol. Res. Lett.* 93, 3121–3134.  
1564 <https://doi.org/10.1785/0220220180>.

1565 Zuza, A., W. Cao, (2020). Seismogenic thickness of California: Implications for thermal  
1566 structure and T seismic hazard *Tectonophysics*, 782 -783, 228426.  
1567 <https://doi.org/10.1016/j.tecto.2020.228426>.